Numerical and Experimental Evaluation of Porosity in High Performance Steel Valve Castings

by
Hendrik Andries Kleynhans

Thesis presented in partial fulfilment of the requirements for the degree of Master of Engineering (Mechanical) in the Faculty of Engineering at Stellenbosch University

Supervisor: Prof. Nawaz Mahomed

March 2018

Declaration

By submitting this thesis electronically, I declare that the entirety of the work contained therein is my own, original work, that I am the sole author thereof (save to the extent explicitly otherwise stated), that reproduction and publication thereof by Stellenbosch University will not infringe any third party rights and that I have not previously in its entirety or in part submitted it for obtaining any qualification.

Date: March 2018

UNIVERSITEIT•STELLENBOSCH•UNIVERSITY
jou kennisvennoot • your knowledge partner

Plagiaatverklaring / Plagiarism *Declaration*

1 Plagiaat is die oorneem en gebruik van die idees, materiaal en ander intellektuele eiendom van ander persone asof dit jou eie werk is.
Plagiarism is the use of ideas, material and other intellectual property of another's work and to present is as my own.

2 Ek erken dat die pleeg van plagiaat 'n strafbare oortreding is aangesien dit 'n vorm van diefstal is.
I agree that plagiarism is a punishable offence because it constitutes theft.

3 Ek verstaan ook dat direkte vertalings plagiaat is.
I also understand that direct translations are plagiarism.

4 Dienooreenkomstig is alle aanhalings en bydraes vanuit enige bron (ingesluit die internet) volledig verwys (erken). Ek erken dat die woordelikse aanhaal van teks sonder aanhalingstekens (selfs al word die bron volledig erken) plagiaat is.
Accordingly all quotations and contributions from any source whatsoever (including the internet) have been cited fully. I understand that the reproduction of text without quotation marks (even when the source is cited) is plagiarism.

5 Ek verklaar dat die werk in hierdie skryfstuk vervat, behalwe waar anders aangedui, my eie oorspronklike werk is en dat ek dit nie vantevore in die geheel of gedeeltelik ingehandig het vir bepunting in hierdie module/werkstuk of 'n ander module/werkstuk nie.
I declare that the work contained in this assignment, except where otherwise stated, is my original work and that I have not previously (in its entirety or in part) submitted it for grading in this module/assignment or another module/assignment.

Studentenommer / *Student number*	**Handtekening / *Signature***
Voorletters en van / *Initials and surname*	**Datum / *Date***

Abstract

The objectives of this study were to develop design and manufacturing process improvement strategies to reduce porosity defects in cast components using simulation technology, as well as to improve the current standards compliance testing procedures for porosity. The research focused on the effect of shrinkage porosity on the quality of cast parts, with the aim of developing a strategy to minimise porosity at the design stage. The strategy is demonstrated in which a (standard compliant) valve body is optimised for minimum porosity using simulation technology. The strategy proved that simulations can be used to improve part quality, reduce casting trials and improve process efficiency.

A commercially available valve, which complied with all the relevant standards and regulations, was investigated for quality on the macro-scale (for macroporosity) using computed tomography (CT) and on the micro-scale (for microporosity) using scanning electron microscopy (SEM). This analysis was conducted to establish the level of porosity in the current design of the component, and to investigate the viability of CT and SEM for porosity inspections. Various porosity defects were identified in the valve component ranging in size, type and distribution density. The most common defects identified were shrinkage porosity, although some other defects, such as sand inclusions and gas porosity, were also present. It is concluded that CT and SEM are viable quality testing methods, although some pitfalls exist in the interpretation of the results. For CT scanning, this includes irregularities, called artifacts, in the results due to an insufficient penetrating power of the scanner. These artifacts can have a similar appearance to microporosity defects.

It is further shown that SEM (with XRD for compositional analysis) can

also prove useful to investigate material compliance with the required material standards, although carbon composition should be interpreted carefully as the technology loses accuracy for lighter elements. The sample preparation process can also have an effect on the carbon composition measurements.

The porosity evaluation of cast components still relies on standard radiographic methods which are subjective in interpretation as it requires comparison of a production radiograph to a reference image without clear classification parameters. An alternative method for standards compliance is proposed which is based on a crack (pore) density formulation. This method requires the calculation of the crack density found in the part, which is then compared to the crack density of the various severity levels given in the reference images of the relevant standard. The study shows that CT and SEM combined with a pore density formulation can provide an objective approach to the classification of porosity severity levels in cast components.

Abstrak

Die doelwitte van hierdie studie was die ontwikkeling van verbeteringstrategieë in die ontwerp- en vervaardigingsproses ten einde tekortkominge in porositeit te verminder deur die gebruik van simulasie tegnologie. Gelyktydig hiermee was 'n verdere doelwit om die toetsprosedures vir porositeit se huidige standaard van gehalte te verbeter. Die navorsing se fokuspunt was op die uitwerking van krimpporositeit op die gehalte van gietstukke met die doel om 'n strategie te ontwikkel wat die porositeit sal minimaliseer tydens die ontwerpfase. Die demonstrasie van die strategie het getoon hoe 'n geskikte klephuis geoptimaliseer is vir minimum porositeit met behulp van simulasie tegnologie. Hierdie strategie het bewys dat simulasies gebruik kan word om onderdeelkwaliteit te verbeter, om die toetsprosesse vir gietstukke te verminder en om die doeltreffendheid van gietprosesse te verbeter.

'n Kommersieel-beskikbare klep wat voldoen het aan al die relevante standaarde en regulasies, se gehalte was ondersoek op die makroskaal (vir makroporositeit) met gebruik van rekenaartomografie (RT) en op die mikroskaal (vir mikro-porositeit) met gebruik van skandering-elektronmikroskopie (SEM). Hierdie analise was gedoen om die huidige ontwerp se porositeit vas te stel asook om die lewensvatbaarheid van RT en SEM in porositeitsondersoeke te bepaal. Verskeie porositeitdefekte was in die klepkomponent is geidentifiseer wat insluit grootte, tipe en verspreidingsdigtheid. Die mees algemene defek wat gevind was, was krimpporositeit. Daar was egter ook ander defekte soos sandinklusies en gasporositeit teenwoordig. Dit was bevind dat RT en SEM geskikte metodes is vir gehalte inspeksie, maar daar bestaan wel sekere vangplekke by die interpretasie van die resultate. By RT skandering is hierdie vangplekke

onreëlmatighede, sogenaamde artefakte, in die resultate as gevolg van onvoldoende deurdringendheidskrag van die skandeerder. Sodanige artefakte kan ooreenstemmend voorkom as mikro-porositeitsdefekte.

Die ondersoeke het verder getoon dat SEM (saam met XRD komposisionele analise) suksesvol gebruik kan word om vas te stel of materiaal aan die vereiste standaarde voldoen. Die koolstofsamestelling moet egter versigtig vertolk word aangesien die tegnologie akkuraatheid vir ligter elemente verloor. Die proses vir monstervoorbereiding kan ook die koolstofsamestelling se afmetings beïnvloed.

Die evaluasie van die porositeit van gietstukke berus steeds op standaard radiografiese metodes waarvan die interpretasie subjektief is, aangesien dit 'n vergelyking vereis van 'n produksie radiograaf met 'n verwysingsbeeld sonder duidelike klassifiseringsriglyne. 'n Alternatiewe metode, gebaseer op die formulering van kraak(porie)digtheidsformulering, vir die voldoening aan standaarde word voorgestel. Hierdie metode vereis die berekening van die gietstuk se kraakdigtheid wat daarna vergelyk word met die kraakdigtheid van die verskillende intensiteitsvlakke van die verwysingsbeelde van die betrokke standaard. Die studie toon dat RT en SEM gekombineer met die formulering van poriedigtheid 'n objektiewe benadering kan voorsien vir die klassifikasie van die intensiteitsvlakke van porositeit in gietkomponente.

Acknowledgements

I would like to express my sincere gratitude to Prof. Nawaz Mohamed for his consistent support and guidance during this research.

Contents

List of Tables

List of Figures

Nomenclature

Acronyms

CD	Crack density
ref	Reference value

Variables

A	Area	$[\mathrm{m}^2]$
c	Specific heat capacity	$[\mathrm{J/kg\ K}]$
G	Temperature gradient	$[\mathrm{K/m}]$
g	Volume fraction	$[-]$
K	Permeability	$[\mathrm{m}^3/\mathrm{s}]$
L	Latent heat of fusion	$[\mathrm{J/kg}]$
P	Pressure	$[\mathrm{N/m}^2]$
T	Temperature	$[\mathrm{K}]$
t	Time	$[\mathrm{s}]$
V	Volume	$[\mathrm{m}^3]$
x	Coordinate	$[\mathrm{m}]$
β	Solidification shrinkage factor	$[-]$
μ	Viscosity	$[\mathrm{Ns/m}^2]$

ρ Density . . . . . $[\mathrm{kg/m^3}]$

Superscripts

* Property evaluated at solidification interface

Subscripts

$_l$ Liquid property

$_s$ Solid property

$_v$ Vapour property

Special Characters

$\mathbf{g}$ Gravity vector . . . . . $[\mathrm{m/s^2}]$

N_y Niyama Value . . . . . $[\mathrm{K^{1/2}min^{1/2}/cm}]$

$\dot{T}$ Cooling rate . . . . . $[\mathrm{K/s}]$

$\mathbf{v}$ Velocity vector . . . . . $[\mathrm{m/s}]$

v_T Solidification interface velocity . . . . . $[\mathrm{m/s}]$

Chapter 1

INTRODUCTION

The casting manufacturing process often results in undesired discontinuities/ defects such as porosity, segregation and phase transformations which have adverse effects on the quality of the final parts. The defects typically occur over a large scale range and are formed by complex mechanisms which complicate the study/classification and even the identification of such defects. Discontinuities such as shrinkage porosity, which is the main focus of this research, and the subsequent effect on part performance are typically not considered in the design process, most likely due to the complexity of such discontinuities. Traditionally, a large safety factor is incorporated into the design, which could add to porosity and other defects and compromise part performance further, as well as add weight to the part. Recently, however, with the advancements of numerical modelling, it has become possible to consider porosity and other discontinuities in the design process, although there is still a lack of confidence from industry, where the traditional casting trials method is the preferred method for porosity mitigation.

1.1 Motivation

Currently, the engineering world is being driven by the need for lighter, more efficient and more economical components and processes while still conforming to the relevant standard and regulations (relevant standards and regulations is discussed in Chapter 2). This makes the design process more complicated, as

will be shown in this research where a high-performance valve that complies with the various standards is designed (Chapter 3) for minimum porosity.

The steel casting process is generally very energy intensive as it requires melting of steel, which has a high melting point and latent heat of fusion. Cast components that do not meet the required standards are scrapped which increases the energy demand due to melting and remelting, adds strain on the upstream processes such as mould and pattern making, as well as the downstream processes such as sand recycling, and notably decreases production efficiency. Improving the casting process at the design stage through simulation and process optimisation is integral in driving the casting industry towards a green manufacturing industry.

Failure of critical components can lead to obvious catastrophic events. Such failure can be accelerated by undetected porosity in the components (the effects of porosity on cast parts are discussed in Section 2). For this reason, a standard compliant valve that is currently used in industry is experimentally investigated using computed tomography and scanning electron microscopy techniques (Section 4) in order to inspect the quality and identify possible improvements in the design.

For this study, a clear distinction is made between macro- and microporosity. In general, the difference between macro- and microporosity is the scale on which they occur, however for this study, the distinction will be defined further:

For experimental investigations, microporosity will be defined as porosity that its smaller than 100×10^{-6} [m], which typically requires microscopy methods to investigate while a pore will be considered macroporosity when its bigger than 100×10^{-6} [m]. Macroporosity can be investigated using various methods such as coventional x-ray and computed tomography techniques.

For numerical optimisation of porosity, micro- and macroporosity will be defined on the same scale as for experimental investigations, although a further distinction is made depending on the method of numerical prediction.

Microporosity is typically predicted using thermal criterion (explained further in Chapter 2) while macroporosity is predicted by explicit solving of the governing equations.

1.2 Research Objectives

The research aims to develop a generalised approach to minimise porosity in castings through optimisation of design and process parameters, and further aims to investigate the use of a quantitative approach, based on the relevant quality standards, for classifying porosity in steel castings.

1.2.1 Minimise porosity in castings with simulation technology

Minimising the porosity in cast components should be a priority, especially when the parts are designed for high-temperature and/or high-pressure service. However, it remains difficult to design for minimum porosity due to the complexity of the solidification process and the geometrical requirements of the design, the relevant standards and regulations and the need for lighter, more efficient and greener components.

Simulation technology has made great advancement since the turn of the century, partly due to the development of new mathematical models as well as the drastic improvement in computing power. The new technology has great power, although the industry has been slow to respond. The first objective of this study is thus to develop a strategy to minimise (or eliminate) porosity in cast components at the design stage, using simulation technology, while still considering the relevant standards, regulations and any other design requirements. This is done in the current study by using a steel valve, as it has complex geometrical features and is required to comply with standards for high temperature and pressure service.

1.2.2 Develop alternative strategy for implementing ASTM-E2868

Compliance with the relevant standards and regulations is important in critical components. It is difficult to classify porosity defects objectively using the current methods for standard compliance as it requires subjective comparison of production radiographs to reference radiographs. Thus, the second objective of this study is to develop a process methodology to investigate compliance for steel valves currently used in industry that is quantifiable and objective.

Chapter 2

LITERATURE REVIEW

2.1 Mathematics of Shrinkage Porosity Modelling

Predicting porosity during solidification is a complex problem involving the modelling of flow in a transient mushy zone, both in terms of moving boundaries and material parameters such as density and permeability. This leads to a highly coupled and (materially) non-linear problem. In the following section, an overview of modelling of shrinkage porosity formation will be discussed from first principles.

2.1.1 Conservation of mass

In a three-dimensional control volume where mass is allowed to cross the boundaries of the control volume, as in Figure 2.1, the conservation of mass for the control volume can be summarised as:

Mass can not be created or destroyed within the control volume, therefore, the rate of change of mass within the control must balance the net influx of mass through the control volume boundaries

In mathematical terms, the conservation of mass can be written in various forms. The most recognised form is the so-called conservative form,

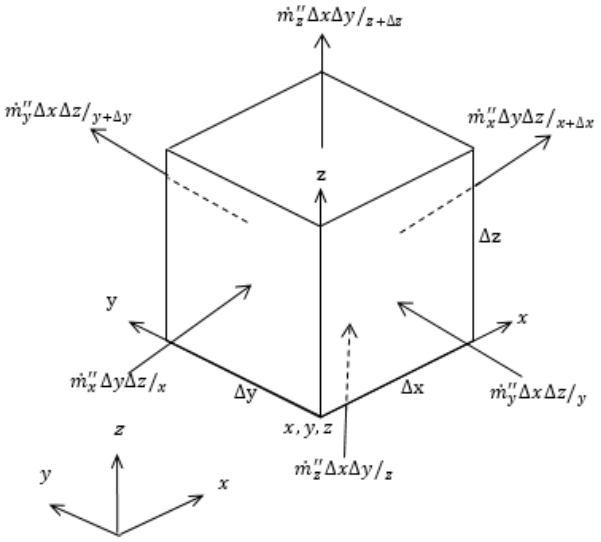

Figure 2.1: Three-dimensional control volume for mass conservation

$$\frac{\partial \rho}{\partial t} + \nabla \cdot (\rho \mathbf{v}) = 0 \tag{2.1}$$

where

ρ is the density and

$\mathbf{v}$ is the velocity vector.

Another useful form, especially for discretisation in numerical schemes is achieved by integrating Equation 2.1 over the control volume V:

$$\int_V \frac{\partial \rho}{\partial t}\, dV + \int_V \nabla \cdot (\rho \mathbf{v})\, dV = 0 \tag{2.2}$$

The first term accounts for the change in density (solidification shrinkage) while the second term accounts for the mass flux through the surfaces of the control volume. Using the divergence theorem, the second term can be converted from a volume integral to a surface integral over the surface A:

$$\int_V \frac{\partial \rho}{\partial t}\, dV + \int_A \rho \mathbf{v} \cdot \mathbf{n}\, dA = 0 \tag{2.3}$$

Equation 2.3 is useful in modelling of casting processes as it is used to perform a mass balance at the solidification interface. In a control volume around the solidification front, as in Figure 2.2, where the superscript "*" indicates that the velocities are evaluated at the solidification front, the control volume moves with the solidification front, and thus, the control volume has velocity $\mathbf{v}^*$.

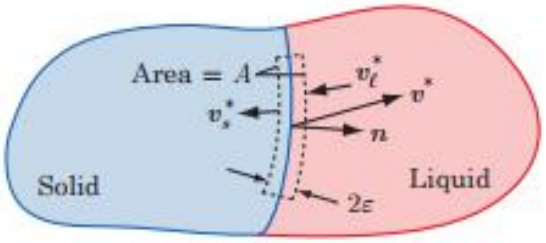

Figure 2.2: Control volume around solidification interface (Dantzig and Rappaz, 2009)

To apply a balance at the interface, the thickness of the control volume must become infinitely small. In the case of an infinitely small thickness, the velocities can all be evaluated at the solidification front.

$$\lim_{\epsilon \to 0}\left(\int_V \frac{\partial \rho}{\partial t}\, dV + \int_A (\rho \mathbf{v}^* \cdot \mathbf{n}\, dA\right) = 0 \tag{2.4}$$

The density at the solidification interface will remain relatively constant, thus the first term falls away. Evaluating the second term, the balance equation for the solidification front becomes:

$$\rho_l A(\mathbf{v}_\mathbf{l}^* - \mathbf{v}^*) \cdot \mathbf{n} - \rho_s A(\mathbf{v}_\mathbf{s}^* - \mathbf{v}^*) \cdot \mathbf{n} \tag{2.5}$$

For porosity modelling, the contraction and deformation of the solid can be ignored i.e. set $\mathbf{v}_\mathbf{s}^* = \mathbf{0}$, which renders Equation 2.5 to:

$$\mathbf{v}_\mathbf{l}^* \cdot \mathbf{n} = \frac{\rho_l - \rho_s}{\rho_l} \mathbf{v}^* \cdot \mathbf{n} = -\beta \mathbf{v}^* \cdot \mathbf{n} \tag{2.6}$$

In the case where the solidification shrinkage factor, $\beta > 0$, as is the case for most materials, it is clear from Equation 2.6 that a liquid will need to flow towards the solidification front in order to compensate for the solidification shrinkage. If there is a lack of flow (say, due to insufficient pressure gradient in the liquid), pores will form in order to satisfy the conservation of mass.

Another useful form of the conservation of mass is the *average form*. The volume average of a arbitrary substance or quantity, Ω is defined as,

$$\langle \Omega \rangle = \frac{1}{V} \int \Omega dV \tag{2.7}$$

From equation 2.7, the average form for the conservation of mass equation is,

$$\frac{\partial \langle \rho \rangle}{\partial t} + \nabla \cdot \langle \rho \mathbf{v} \rangle = 0 \tag{2.8}$$

where the average density, $\langle \rho \rangle$, is defined as,

$$\langle \rho \rangle = \rho_l g_l + \rho_p g_p + \sum \rho_v g_v = \rho_l g_l + \rho_p g_p + \langle \rho \rangle_s g_s \tag{2.9}$$

where g_l, g_p and g_s, refer to the volume fraction of liquid, void and solid phases respectively.

The average velocity, $\langle \rho \mathbf{v} \rangle$ is defined as,

$$\langle \rho \mathbf{v} \rangle = \rho_l g_l \langle \mathbf{v} \rangle_l + \langle \rho \rangle_s g_s \langle \mathbf{v} \rangle_s \tag{2.10}$$

When using the definitions of average density and velocity, Equation 2.8 becomes:

$$\frac{\partial\langle\rho_0\rangle}{\partial t} - \rho_l\frac{\partial g_p}{\partial t} + \nabla\cdot(\rho_l g_l\langle\mathbf{v}\rangle_l) + \nabla\cdot(\langle\rho\rangle g_s\mathbf{v}_s) = 0 \tag{2.11}$$

In Equation 2.11, the first term quantifies the total amount of solidification (and thermal) shrinkage. The shrinkage is balanced by either pore growth (second term), or fluid flow into the dendritic area. The last term in Equation 2.11 can add to solidification shrinkage but will lead to other defects such as deformation and hot tears, and can thus be ignored when predicting porosity. The relevant equation to porosity modelling becomes:

$$\frac{\partial\langle\rho_0\rangle}{\partial t} + \nabla\cdot(\rho_l g_l\langle\mathbf{v}\rangle_l) = \rho_l\frac{\partial g_p}{\partial t} \tag{2.12}$$

2.1.2 Conservation of momentum

The velocity field and pore fraction is unknown in Equation 2.12. The velocity field is coupled to the pressure drop through the interdendritic zone (mushy zone). This pressure-velocity coupling is critical to accurately model any flow field and is discussed in depth in the text of Versteeg and Malalasekera (2007). In solidification modelling, the mushy zone is treated as a porous medium. The conservation of momentum is used, in conjunction with a semi-empirical relationship (Kozeny-Carman model) to model the permeability variations due to an increasing solid fraction, in order to solve the pressure-velocity coupling in the mushy zone. This gives the well-known Darcy form (discussed in details in the text of Dantzig and Rappaz (2009)).

$$\langle\mathbf{v}_l\rangle = g_l\langle\mathbf{v}\rangle_l = \frac{-K}{\mu}(\nabla P_l - \rho_l\mathbf{g}) \tag{2.13}$$

In Equation 2.13, $\mathbf{g}$ is the gravity field and K the permeability. Combining the conservation of mass and conservation of momentum equation, and ignoring the void growth, results in the second order partial differential equation:

$$\nabla \cdot (\rho_l \frac{K}{\mu_l}(\nabla P_l - \rho_l \mathbf{g})) = \frac{\partial \langle \rho_0 \rangle}{\partial t} \tag{2.14}$$

Ignoring the void growth simplifies the mathematics, while the argument is made that void growth will not significantly influence the pressure-velocity field since the relative void fraction is low compared to the solid and liquid fractions in casting applications. It is clear from the formulation above, that the pressure drop through the mushy zone will have a significant effect on the porosity formation. Modelling of pressure drop in the mushy zone is computationally expensive as the mushy zone is not on the same scale as the castings.

Equation 2.14 can be solved with the correct boundary conditions, i.e at the extreme ends of the mushy zone where the solid fractions will be either 0 or 1. The most common implementation of the boundary conditions leads to the Niyama criterion - a one-dimensional criterion function to predict shrinkage porosity.

2.1.3 Niyama and other thermal criteria

In a one-dimensional solidification interface, as in Figure 2.3, with the mass balance at the solidification interface (Equation 2.6) the flow induced by solidification shrinkage is related to the solidification shrinkage factor, β, and the velocity of the solidification front, $\mathbf{v}^*$. In one-dimension, with a solidification front velocity $\mathbf{v}^* = v_T$, the conservation of mass is:

$$\frac{\partial \langle \rho_0 \rangle}{\partial t} + \frac{\partial (g_l \rho_l \langle \mathbf{v} \rangle_{lx})}{\partial x} = 0 \tag{2.15}$$

$$\frac{\partial \langle \rho_0 \rangle}{\partial t} + v_T \frac{\partial \langle \rho_0 \rangle}{\partial x} = 0 \tag{2.16}$$

Combining these equations results in,

$$v_T \frac{\partial \langle \rho_0 \rangle}{\partial x} = \frac{\partial (g_l \rho_l \langle \mathbf{v} \rangle_{lx}}{\partial x} \tag{2.17}$$

which implies that,

$$-v_T\langle\rho_0\rangle + g_l\rho_l\langle v\rangle_{lx} = constant \tag{2.18}$$

In order to apply sensible boundary conditions, it is assumed that the density of the liquid and solid is constant but not equal to one another. This allows a simple formulation of the average density as:

$$\langle\rho_0\rangle = g_s\rho_s + g_l\rho_l \tag{2.19}$$

Applying the boundary condition at the root of the dendrites ($g_l = 0$), the constant can be determined:

$$-v_T\langle\rho_0\rangle + g_l\rho_l\langle v\rangle_{lx} = constant = -\rho_s v_T \tag{2.20}$$

Next, applying the boundary condition at the tip of the dendrites ($g_s = 0$), results in:

$$\rho_l(\langle v\rangle_{lx} - v_T) = -v_T\rho_s \tag{2.21}$$

$$\langle v\rangle_{lx} = v_T - \frac{v_T\rho_s}{\rho_l} = -\beta v_T \tag{2.22}$$

This relationship is shown visually in Figure 2.3.

Using this relationship in the original Darcy equation in the absence of gravity (Equation 2.13 with $\mathbf{g} = 0$) an expression for the pressure drop in the mushy zone can be derived as follows:

$$\frac{\partial P}{\partial x} = \beta v_T \mu_l \frac{g_l(x)}{K(g_l(x))} \tag{2.23}$$

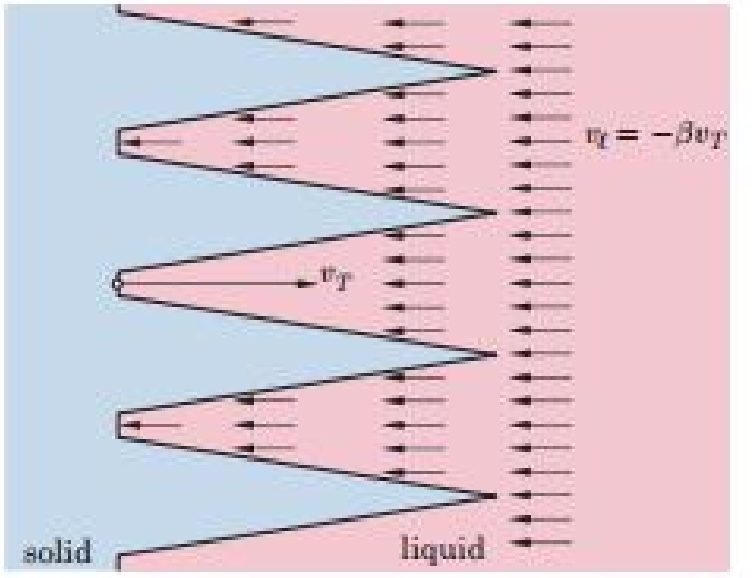

Figure 2.3: One-dimensional solidification interface with columnar growth (Dantzig and Rappaz, 2009)

$$\Delta P = \beta v_T \mu_l \int_x^{x_tip} \frac{g_l(x)}{K(g_l(x))} dx \tag{2.24}$$

The pressure drop in the mushy zone is thus proportional to the solidification shrinkage factor, the viscosity and the velocity of the interface. The solidification shrinkage factor and viscosity is defined by the type of material while the velocity can be influenced by process conditions such as cooling rates. Niyama *et al.* (1982) recognised that measuring the v_T is difficult in practice. They then replaced the velocity with a ratio between the thermal gradient and the cooling rate.

$$v_T = -\frac{\dot{T}}{G} \tag{2.25}$$

Experiments by Niyama *et al.* (1982) showed that shrinkage porosity occurs in steels when:

$$N_y = \frac{G}{\sqrt{-\dot{T}}} < 1 \tag{2.26}$$

Equation 2.26 is known as the Niyama criterion and falls under the broader category of thermal criterions, usually a function of thermal gradients, cooling rates and solidification front velocities. The Niyama criterion is an improvement on the so-called Pellini criterion which only depends on the thermal gradient and is dependent on the shape (size and complexity) of the casting (Tavakoli, 2014).

Carlson and Beckermann (2008) investigated the use of the Niyama criterion for shrinkage defects prediction in Nickel alloy castings by simulating the filling and solidification and correlating the Niyama values with (micro an macro) porosity containing areas. They found that macroporosity, visible on radiographs correlates, to Niyama values, $N_y < 1$, but also found that microporosity occurs at higher Niyama values, $N_y < 2$, for the nickel-based alloys used in their study. They concluded that critical areas in a casting should have Niyama values of at least $N_y > 2$ to be a sound casting.

In another study, the same authors (Carlson and Beckermann, 2009*b*), developed a dimensionless Niyama criterion. The reasoning behind the dimensionless criterion is to avoid the need for threshold values which are material dependent. Although they found some success with this criterion, it has been criticised by Sigworth (2009) and, to some extent, by Tavakoli (2014). In a reply to Sigworth's criticisms, Carlson and Beckermann (2009*a*) disproved much of Sigworth's claims. Despite this, the dimensionless Niyama criterion has not been used extensively in industry or in research.

Stefanescu (2005) found that thermal criterion functions can be used in ferrous castings but it should be noted that other forms of porosity, such as gas porosity will not be predicted with these criterions. Many researchers have used the Niyama criterion to predict porosity, both macro and micro. For example Li *et al.* (2014) used the Niyama criterion to successfully predict microporosity in WE54 Alloy castings. Finally, it should be noted that the

Niyama criterion and other thermal criterion are mainly qualitative indicators, and can thus not be used to quantify porosity.

2.2 Porosity Classification

Shrinkage porosity can take various forms and are always dictated by the geometry of the part and gravity i.e. by a lack of feeding to the solidification interface. Campbell (2003) classifies shrinkage porosity in his text as seen in Figure 2.4. He classified different types of shrinkage porosity as:

(a) Centreline porosity, which usually forms parallel to the thermal axis and in the general area of a feeder that does not provide sufficient feeding.

(b) Sponge porosity, which is usually found in alloys with long freezing ranges and part with sufficient temperature gradient and insufficient feeding.

(c) Layered porosity, which is usually found in parts with insufficient inter-dendritic feeding and insufficient thermal gradient.

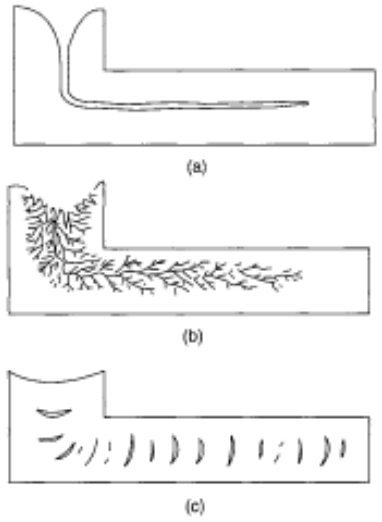

Figure 2.4: Campbell (2003)

Porosity must be classified according to type and severity to determine whether a part is suitable for certain applications. ASTM-E446-14 (2013) pro-

vides reference radiographs of various discontinuities or defects (summarized in Table 2.1) found in castings with levels of severity for each type of defect, while the digital format of the radiographs are provided in ASTM-E2868 (2013).

Table 2.1: List of casting defects reference radiographs provided by ASTM-E446-14 (2013) and ASTM-E2868 (2013)

Category	Description	Severity levels
A	Gas porosity	1-5
B	Sand and slag inclusions	1-5
C_a	Linear shrinkage	1-5
C_b	Feathery shrinkage	1-5
C_c	Sponge shrinkage	1-5
C_d	Combinations of all shrinkage	1-5
D	Crack	1
E	Hot tear	1
F	Insert	1
G	Mottling	1

2.3 ASME-B16 Compliance

The "American Society of Mechanical Engineers" (ASME), has a sub committee (Committee B16) which specifically deals with the standardisation of valves, fittings, and gaskets. The committee provides various standards to which the design, manufacturing, and testing of valves should comply with, in order to be suitable for certain applications. The most relevant to this research is ASME-B16.34.

ASME-B16.34 (2013) prescribes acceptable defect levels for a valve to be accepted as in Table 2.3. The procedure for classifying the severity of a defect is performed radiographically with reference radiographs for each severity level given in ASTM-E446-14 (2013). These radiographs are available in a digital format, given in ASTM-E2868 (2013).

Table 2.2: Acceptable defect category for ASME B16.34 compliance (ASME-B16.34, 2013)

Defect type	Category	Acceptable severity
Gas	A	2
Sand and slag	B	3
Linear shrinkage	C_a	2
Feathery shrinkage	C_b	3
Sponge shrinkage	C_c	3
Combinations shrinkage	C_d	3
Hot tears and cracks	D, E	
Inserts	F	

2.4 Defect Severity Classification Procedure in ASTM-E2868

The evaluation procedure is prescribed in Section 7 of (ASTM-E2868, 2013). Reference images or radiographs for the various types of defects and severities (see Table 2.1). The procedure requires comparison radiographs of a production part to be compared with these reference images in order to determine the defect type and severity level.

Carlson *et al.* (2001) did a statistical study to determine the repeatability of shrinkage defect ratings and classification (in terms of type and severity) with the procedure prescribed in ASTM-E2868 (2013). It was found that there was only a 12,5 % unanimous agreement for both shrinkage type and severity level. All of the x-rays containing a severity level of either one or five had unanimous agreement, however, severity levels two, three and four had variance up to 2 levels. In the same study, an alternative method is suggested which is discussed in Chapter 5 along with a the proposed strategy developed in this research.

2.5 Experimental Methods for Porosity Identification/Quantification

Porosity and other defects/discontinuities in castings are typically not visible to the naked eye unless on the surface of a part. However, they can still be difficult to identify due to the scale of the defects and other factors such as surface finish of cast parts. There are various methods available to visualise defects on castings. Surface cracks and porosities can be identified using non-destructive methods such a liquid penetrant testing. Internal defects are not as simple as it might require destruction of the part in order to perform accurate radiographic scans or to investigate microscopic features using microscopy.

2.5.1 X-ray computed tomography

The technology of x-ray computed tomography was developed in the early 1970's by Cormack (1973) when the technology was envisioned to be used in the medical industry. It did not take long before the power of the technology in non-medical applications was recognised, for example, non-destructive evaluation (NDE) of industrial parts (Gilboy, 1984). The technology has been used by industries such as Boeing to analyse cast components since the 1990's (Bossi and Georgeson, 1992). The technology has improved drastically over the past decades with the advancement of computer power and is now an obvious choice for NDE or testing of a wide variety of materials and part sizes as was recently shown by Du Plessis *et al.* (2016*b*).

Computed tomography has been used in casting related investigations in the last decade to:

Identify internal discontinuities: In the past, internal discontinuities were difficult to identify without the use of destructive methods. With computed tomography, these discontinuities can be identified in terms of size and location, and depending on the material, geometry and the scanning power, the tests can be completed non-destructively. Bednarz and Szwedowicz (2015) used computed tomography to develop a low-cycle fatigue assessment strategy

for alloys containing microporosity in order to understand the effect of microporosity on performance (see Section 2.6) and to reduce product development costs. Hardin and Beckermann successfully used computed tomography to investigate the internal defects of castings and the effect of these defects on the mechanical and material properties of the parts (Hardin and Beckermann, 2007, 2009, 2012, 2013).

Verify geometrical features: Solidification and cooling of castings usually lead to some sort of deformation of the final product. With the use of computed tomography, the variance between the design file and the cast product can be quantified. Du Plessis and Rossouw (2015) applied CT for dimensional quality control of titanium components used in the aerospace industry.

Computed tomography can also be used to confirm standard compliance in terms of geometrical features such as wall thickness and fillet radii, as was shown by Müller *et al.* (2013), who used computed tomography to verify tolerances of industrial parts. It is recognised, however, that such testing can become expensive and is not always possible to perform non-destructively, especially for parts made from high-density material (such as steel valves) as CT scanners require more power to penetrate higher density materials compared to lower density materials.

Verify simulation results: Simulation technology has improved drastically since the first finite difference models were implemented at the end of the previous century. However, there is still some discussion on the accuracy of results using simulations, especially for complex phenomenon such as solidification. Computed tomography provides the capabilities to verify numerical/simulation results in terms of internal discontinuities as well as distortion after solidification and cooling.

Hardin and Beckermann (2007, 2009, 2012, 2013); Du Plessis *et al.* (2017) and Amirirad *et al.* (2014) successfully showed how computed tomography scans can be incorporated to predict the performance of cast parts in service. This was shown by performing finite element analysis on the computed tomography scans, which included the (macro) defects left by the casting process.

2.5.2 Scanning electron microscopy

Scanning electron microscopy is a versatile technology with great potential for casting micro-features inspection. Some of the relevant capabilities of SEM for this research are:

Investigation of microstructure: The solidification process has a direct effect on the subsequent micro-structure of the material such as the grain size and phase formation. Certain phases are detrimental to part performance and a heat treatment protocol is often needed to ensure the correct phases are present in the part. Cupido *et al.* (2015) investigated the affect heat treatment on the microstructural evolution of a sand cast aluminium alloy using SEM. Rzyankina *et al.* (2013) showed how SEM can be used to investigate the grain structure in cast turbine blades.

Identifying microporosity: The detrimental effect of microporosity is discussed in Section 2.6. The scale of microporosity requires investigation by some form of microscope. As was previously mentioned, Li *et al.* (2014) successfully used SEM to identify and classify microporosity in WE54 Alloy casting.

Verify simulation results: The use of simulations can predict microporosity formation as well as phase formations and grain structures. SEM allows for verification of these predictions and can build confidence in the technology as was shown by Li *et al.* (2014).

2.6 Material and mechanical properties

A valve investigated in this research (see Section 4) is cast from ASTM-A216 WCB steel. The prescribed composition for this material is summarised in Table 2.3. The steel has a good balance between ductility and strength (245 [MPa] yield strength and 485 [MPa] tensile strength). This material is used throughout the current study.

Table 2.3: Maximum chemical composition of A216 WCB steel (ASTM-A216, 2014)

Element	Composition [wt%]
Carbon [C]	0.3
Manganese [Mn]	1.00
Phosphorus [P]	0.035
Sulphur [S]	0.035
Silicon [Si]	0.60
Residual elements:	
Copper [Cu]	0.30
Nickel [Ni]	0.50
Chromium [Cr]	0.50
Molybdenum [Mb]	0.20
Vanadium [V]	0.03

The effect of porosity on the mechanical performance of cast steel has not been well established and has been the subject of various studies. Hardin and Beckermann (2007) conducted an experimental investigation using tensile specimens to study the effect of macroporosity on the stiffness of cast steel. They found that the stiffness of a material is reduced with increased porosity and that the material loses all stiffness above a critical porosity level. The data from this study is summarised in Figures 2.5 with a best-fit model applied to the data. The fit parameters are summarised in Table 2.4. The porosity distribution for each specimen was recorded using computed tomography (see Section 2.5) and incorporated into finite element analysis where the strain in the specimen was predicted acceptably. Ol'khovik (2015) found similar results.

Hardin and Beckermann (2009) applied the same strategy to investigate the effect of porosity on the fatigue of the specimen. The data is presented in Figure 2.6, again with a best-fit model applied to the data, summarised in Table 2.5. The porosity clearly has a detrimental effect on the fatigue life of the specimens. Sigl *et al.* (2004) also investigated the fatigue resistance of cast steel with porosity and found that porosity influences the fatigue resistance of cast steel. The script for the best-fit model of Figured 2.5 and 2.6 is given in Appendix A.

Hardin and Beckermann (2013) found that ultimate tensile strength is

affected to a lesser degree when compared to the ductility and fatigue life. Ol'khovik (2015) showed that the yield strength is reduced linearly as a function of the amount of porosity in the cast material. Susan *et al.* (2015) also found that the ductility is influenced more severely compared to the the tensile and yield strength of investment cast stainless steel.

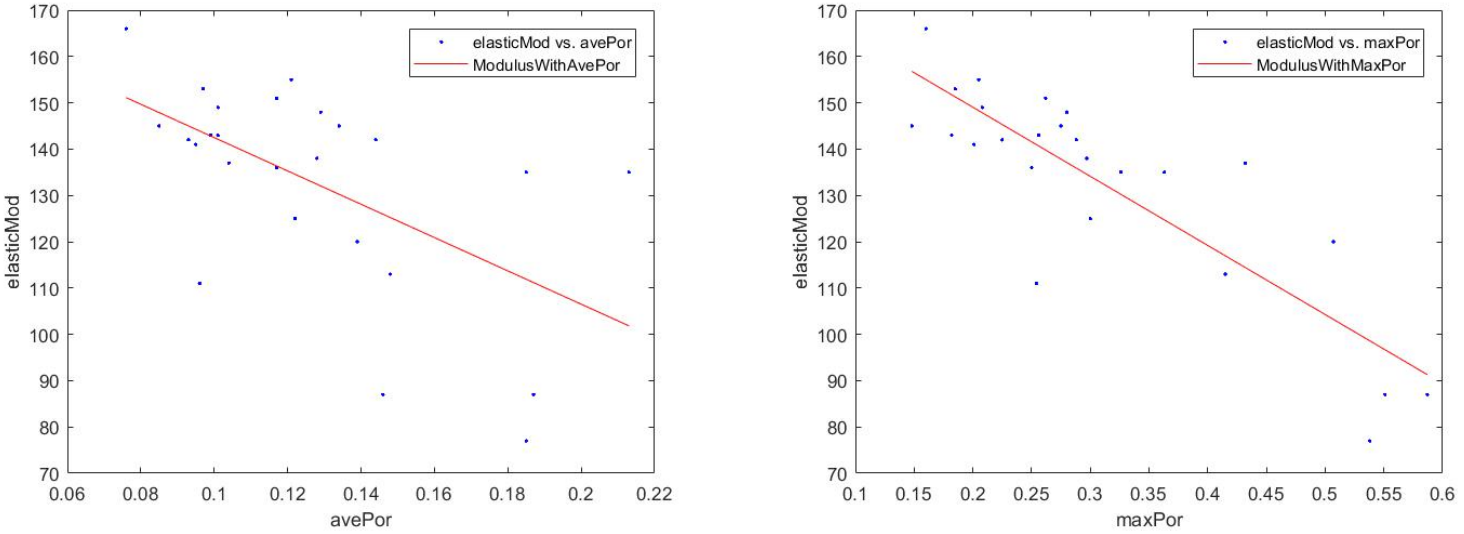

Figure 2.5: Elastic modulus reduction as a function of average and maximum porosity respectively from (Hardin and Beckermann, 2007)

Table 2.4: Best-fit data for Figure 2.5

Figure	Model	R^2	Coefficients
E-mod vs ave por	$y = ax + c$	0.33	$a = -359.8,\ c = 178.5$
E-mod vs max por	$y = ax + c$	0.72	$a = -19.04,\ c = 133$

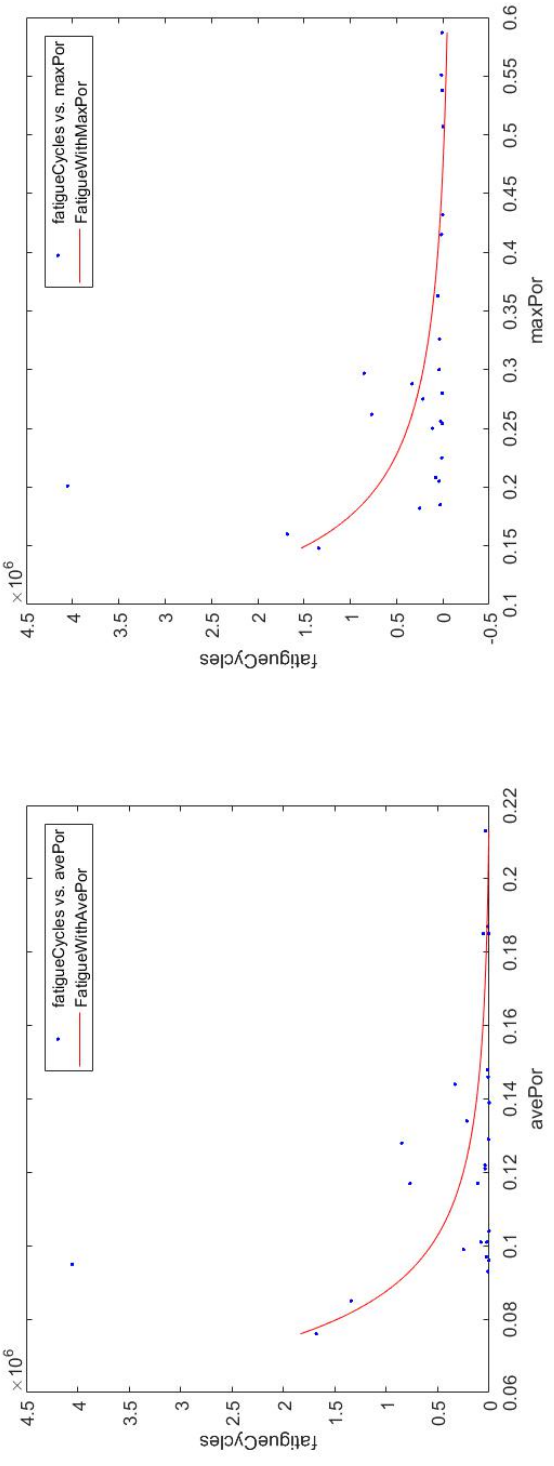

Figure 2.6: Elastic modulus reduction as a function of average and maximum porosity respectively from (Hardin and Beckermann, 2007)

Table 2.5: Best-fit data for Figure 2.6

Figure	Model	R^2	Coefficients
Fatigue vs ave por	$y = ax^b + c$	0.23	$a = 37.67,\ b = -4.193,\ c = -2.1 * 10^4$
Fatigue vs max por	$y = ax^b + c$	0.22	$a = -2.138 * 10^4,\ b = -2.274,\ c = -1.168 * 10^5$

Chapter 3

NUMERICAL OPTIMISATION OF VALVE QUALITY

The advancement of computational power since the turn of the century has made it possible to numerically solve large systems of equations. The governing physics of the casting process can be discretised to form such systems of equations which allows for numerical prediction of the casting process. This chapter uses simulation technology to improve the quality of cast components with the following objectives in mind:

- Design a gate valve body for minimum porosity that is compliant with the regulations set out in ASME-B16.34 (2013), ASME-B16.10 (2017) and API-600 (2015) and using simulation technology.
- Investigate critical (and non-critical) parameters in valve design using simulation technology. These parameters can be geometrical or/and process related.

The numerical investigation starts with a mesh independence study, followed by a optimisation study and concludes with a complete simulation of the casting from filling to cooling.

3.1 Design with Simulation

As mentioned in previous sections, the geometrical design of a valve must comply with certain standards. The standards prescribe geometrical features such as minimum wall thickness, flange thickness, overall distances (flange to flange etc). The standard does not allow much freedom for design; however, it is shown in the following that minimal changes in the geometry (that still complies with the standards) can drastically reduce the porosity of the valve.

The simulation set-up is a critical step in any numerical investigation as it can have a direct influence on the results.

3.1.1 Hardware and software details

The software available for this research is MAGMA-GmbH (2017) which is commercially available. Magmasoft© uses a finite volume method with a multi-phase model in the discretisation of the relevant governing equations for porosity formation.

The multi-phase model, described in Carlson *et al.* (2002) and Carlson *et al.* (2006), calculates the energy, mass and momentum conservation equations:

$$(\rho c - \rho L \frac{dg_s}{dT}) \frac{\partial T}{\partial t} = \nabla \cdot (k \nabla T) \tag{3.1}$$

$$\frac{\partial}{\partial t}(g_s \rho_s + g_l \rho_l + g_p \rho_p) + \nabla \cdot (\rho_l \mathbf{v}) = 0 \tag{3.2}$$

$$\nabla^2 \mathbf{v} = \frac{g_l}{K}\mathbf{v} + \frac{g_l}{\mu_l}\nabla P - \frac{g_l}{\mu_l}\rho_{ref}\mathbf{g} \tag{3.3}$$

In the mushy zone, the superficial velocity, $\mathbf{v}$, becomes very small which reduces Equation 3.3 to the Darcy equation discussed in Section 2.

The software license available to this research allowed for the simultaneous use of four central processing units. A full filling, solidification and stress

simulation for the valve body requires in excess of 3 days to complete, therefore, the optimisation study can only focus on solidification as it requires in the order of 300 simulations (which would require in excess of 900 days to complete). Once the optimisation is completed, a single filling, solidification, and stress simulation is performed.

3.1.2 Mesh independence

As discussed in Section 2, when working with numerical schemes, there will always be an error in the results, mostly due to discretisation techniques, numerical solving schemes and boundary conditions.

Magmasoft© does not use dynamic meshing techniques. In an effort to minimise the error in the results, mesh independence must be established. This ensures that the results are not dependent on the mesh used. There will however still be some finite error in the results. Filling and solidification are considered in the mesh independence study. An example mesh is shown in Figure 3.1.

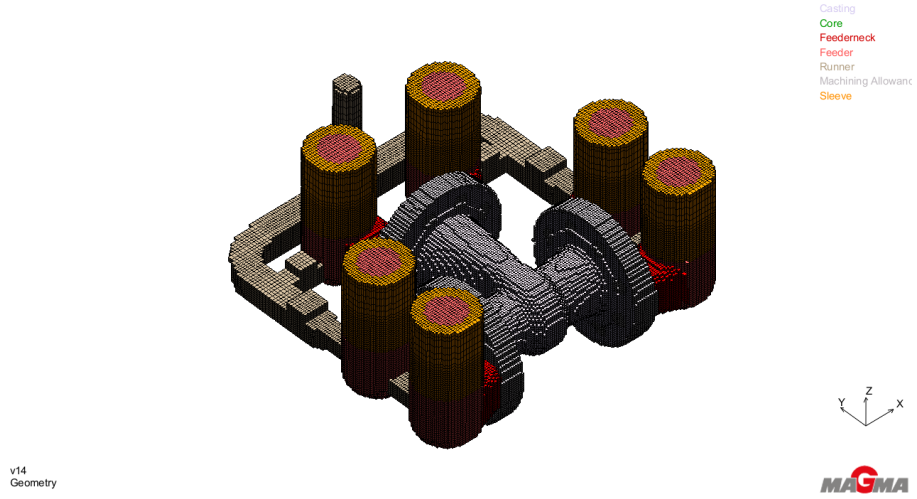

Figure 3.1: Coarse mesh used for mesh independence study

In order to confirm mesh independence, three simulations were performed on three refined meshes. The mesh and simulation details are summarised in Table 3.1.

Table 3.1: Mesh and simulation details for independence study

Mesh	Element size	No. Elements	Sim time
Coarse	3 mm	1 685 398	3h 47m
Medium	2.5 mm	2 203 200	4h 37m
Fine	2 mm	2 558 160	5h 25m

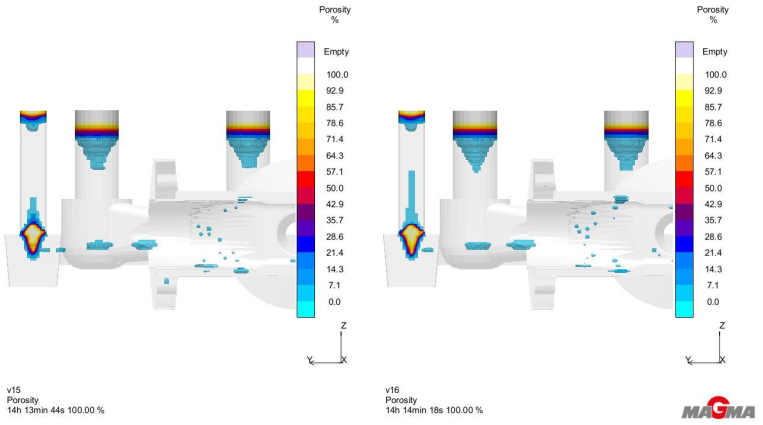

Figure 3.2: Visual representation of mesh independence by porosity prediction for two refined meshes

The temperature history for the mean temperature of the cast material is recorded during each simulation and plotted in Figure 3.3. Microporosity formation is predicted from the Niyama criterion which is a function of temperature only and thus the mesh independence study only considered temperature history. From this data, mesh independence is confirmed. Visually, mesh independence if further confirmed in Figure 3.2 which shows the porosity prediction for two mesh refinements.

The maximum and minimum temperature history for three successively refined meshes are given in Appendix B in an effort to further confirm mesh independence.

3.1.3 Material specification

The ASTM standard regulates the compositional variance allowed in the A216-class steel as specified in Chapter 2, however, for the simulation, specific values must be used. The steel properties used in the simulation is summarised in

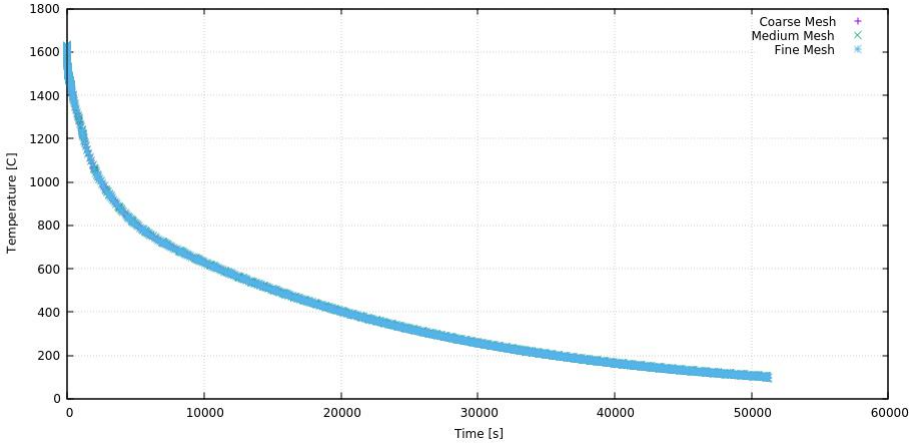

Figure 3.3: Mean temperature history in cast material for three refined meshes

Table 3.2.

The valve body is cast in a sand mould. Various options are available when it comes to the type of sand used for the mould and core. In the experimental investigation, some silica sand inclusions were found and is therefore the obvious choice for the simulation. The details required for the simulation with regards to the silica sand is specified in Table 3.3.

Table 3.2: Material specification on A216 on Magmasoft© database

Material property	**Value**
Liquidus temperature	1519 °C
Solidus temperature	1412 °C
Niyama criterion temperature	1422.7 °C
Feeding effectivity	30 %
Surface tension coefficient	1.5 N/m
Composition [wt%]	
Carbon (C)	0.24
Manganese (Mn)	1.1
Phosphorus (P)	0.035
Sulfur (S)	0.035
Silicon (Si)	0.5

Table 3.3: Material properties for silica sand used in mould and core

Property	Value
Permeability	50 cm^3/min
Grain diameter	0.24 mm
Grain density	2650 kg/m^3

3.2 Optimisation and Design for Quality with Respect to Porosity

One of the main aims linked, to the first objective of this research, is to determine which parameters (process and geometrical) has a significant effect on the quality of the cast valves. The optimisation study can only focus on solidification due to hardware and time constraints, thus the following geometrical and process parameters are chosen to be used in the optimisation. The details of the variable parameters are summarised in Table 3.4.

In an effort to improve simulation time, the symmetry boundary condition is applied as shown in Figure 3.4. As there is no filling, and thus no reason for non-symmetrical behaviour, this simplification will not have an effect on the final results of the optimisation.

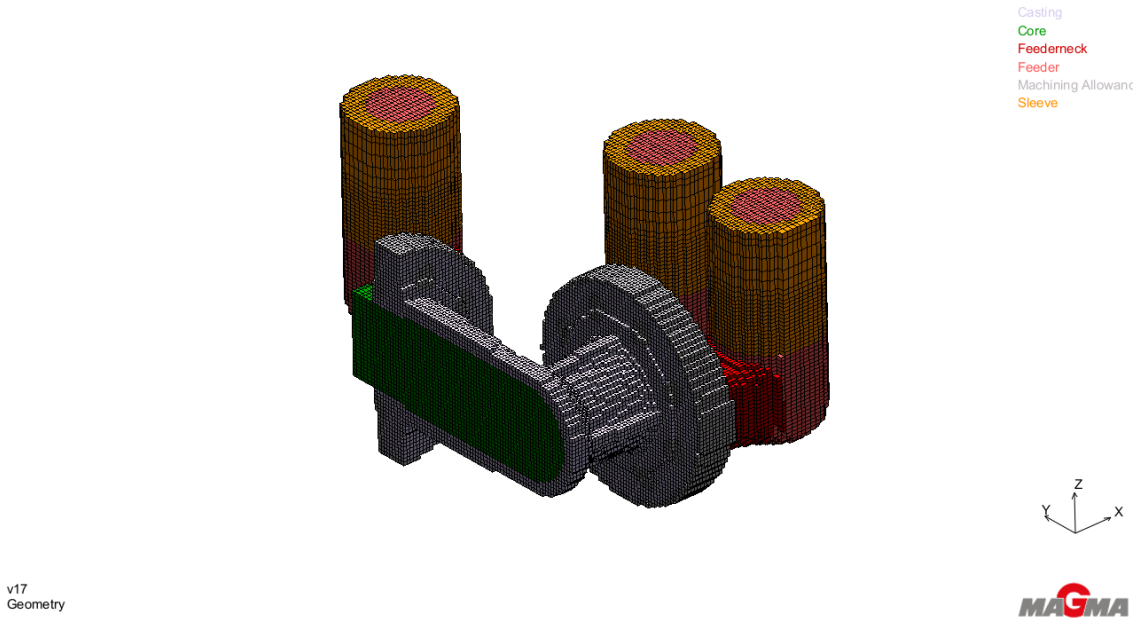

Figure 3.4: Mesh details showing use of symmetry

3.2.1 Parameters and increments

Process: Initial temperature - The temperature of the melt is the only process parameter that can be changed when only considering solidification. It is expected that the temperature of the melt will have an effect on the feeding of the mushy zone. The temperature will also influence the total shrinkage/contraction potential of the casting.

Geometry: Machining thickness of flow section (MT) - Owing to the contraction of a casting, the casting design must be bigger than the minimum wall thickness prescribed in ASME B16.34. This excess wall thickness can be used to the advantage in terms of design as it can provide feeding to critical areas in the valve during solidification. The machining thickness is displayed (with a taper) in Figure 3.5.

Geometry: Flow section taper (SP) - A strategic taper is added to the machining thickness to ensure the critical area solidifies first and has sufficient feeding. The starting point of the taper section will have an effect on the taper

angle as well as the amount of post cast machining required after casting. The starting point of the taper can be seen in Figure 3.6.

Geometry: Machining thickness of spindle section (R) - As for the wall thickness of the flow section, the spindle section wall thickness is given a taper by adjusting the radii of the core (see Figure3.7). This section will not require machining after casting, however, the parameter will add to the amount of material needed for the valve body, which has cost implications.

Geometry: Rib Geometry (RWB, RWH) - The valve investigated in Chapter 4, has ribs along the outside of the flow section as seen in Figure 4.1. These ribs are added to the optimisation to investigate their effect on the quality of the part. The number of ribs is also added as a parameter to ensure completeness.

A full section view of the valve is shown in Figure 3.8 which gives context to Figures 3.5 - 3.7.

Table 3.4: Optimisation set up and parameter values

Optimization parameters		
Parameter	**Range**	**Step**
Initial temperature	1450 °C to 1630 °C	15 °C
Machining thickness (MT)	14 mm to 19 mm	1 mm
Flow taper (SP)	50 mm to 100 mm	10 mm
Spindle taper (R)	34 mm to 40 mm	2 mm
RWB	10 mm to 15 mm	2.5 mm
RWB_2	15 mm to 20 mm	2.5 mm
RHB	2.5 mm to 10 mm	2.5 mm
RHB_2	10 mm - 20 mm	5 mm
No. Ribs	0-4	1
Simulation parameters		
Parameter		**Details**
Possible designs		326592
Generations		16
Generation size		22
Optimization size		352
Mesh size		3 mm
No. of element		854 568
Simulation time		19h 7m

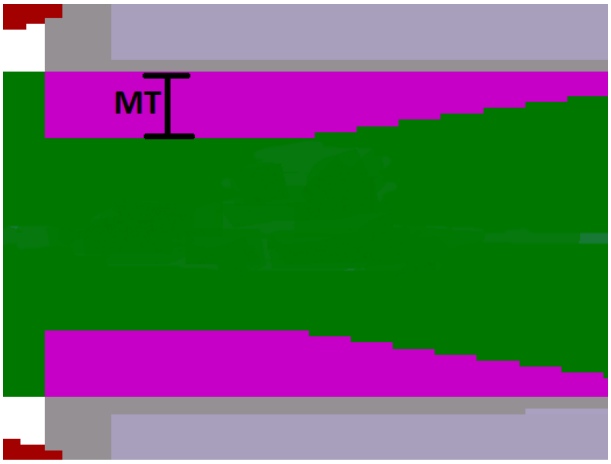

Figure 3.5: Machining thickness (MT) of flow section definition for optimisation

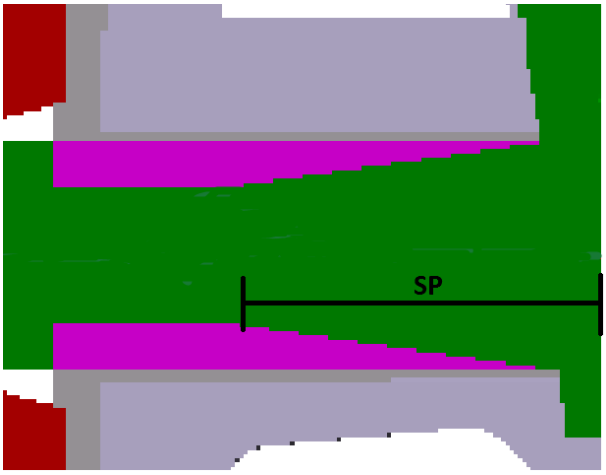

Figure 3.6: Starting point (SP) of flow section definition for optimisation

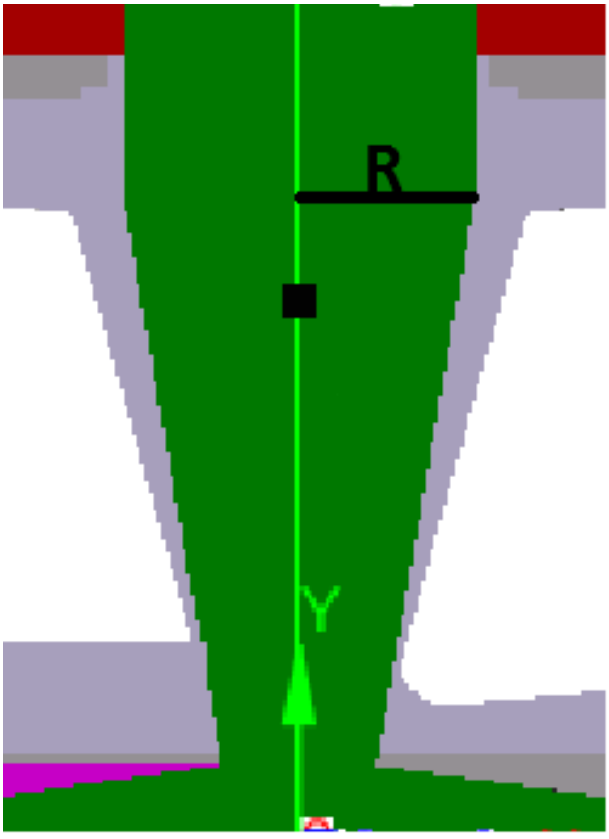

Figure 3.7: Radius of spindle section definition for optimisation

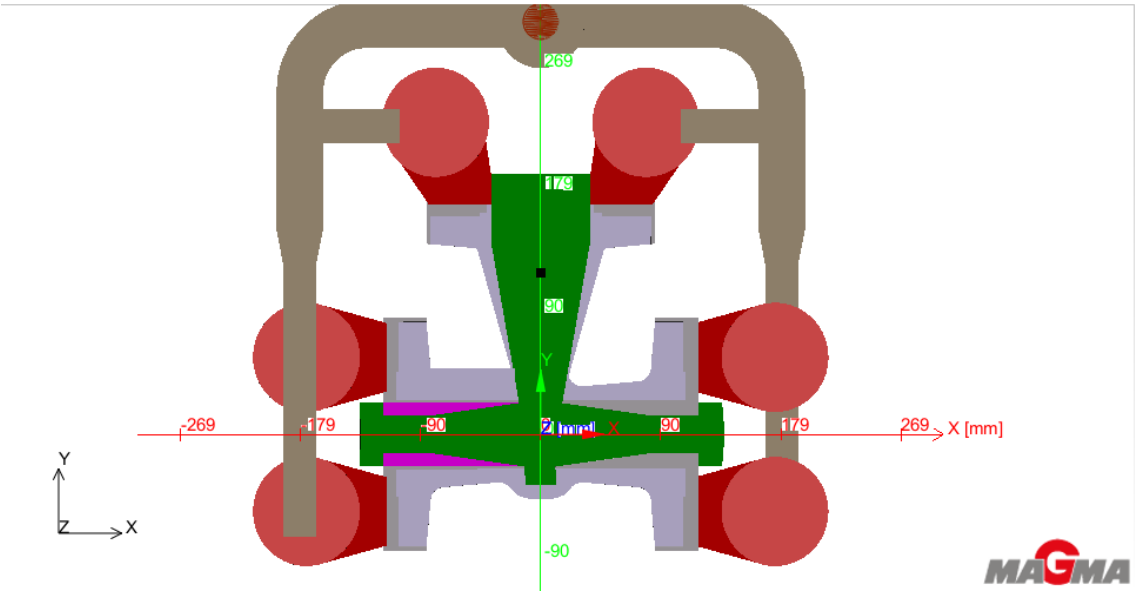

Figure 3.8: Full section view of valve body geometrical features

3.2.2 Optimisation objectives

Magmasoft© allows various objectives to be specified that will drive the direction of the optimisation. This capability should be used with caution as different objectives and objective combinations will have different optimal solutions in the design space. The objectives should align with one another to give the algorithm the best chance to converge towards an optimal solution. For instance, setting an objective to reduce porosity and other to increase yield will cause the objectives to work against one another, and the algorithm will converge to a different area in the design space. It should be noted that this study is not necessarily interested in the absolute optimal solution, but rather to investigate which parameters have the most significant impact on the porosity of the valve.

The objective of this investigation is chosen as follows (definition for the critical area is shown in Figure 3.9):

Reduce porosity: This objective is the main driving force of the optimisation procedure and will look to reduce to overall porosity in the valve.

Max microporosity (in critical area): This objective only considers the max value of the microporosity in the critical area and will look for designs that reduce the maximum value.

Average microporosity (in critical area): Similar to the maximum microporosity, this objective evaluates the average microporosity in the critical area and attempts to find a design that minimises the average microporosity.

Maximum macroporosity: As macroporosity has more significant effect on the performance of the valve, this objective is set to minimise the maximum value of macroporosity in the entire valve. Only macroporosity is considered in the relevant standards, therefore, reducing maximum macroporosity should be the first priority.

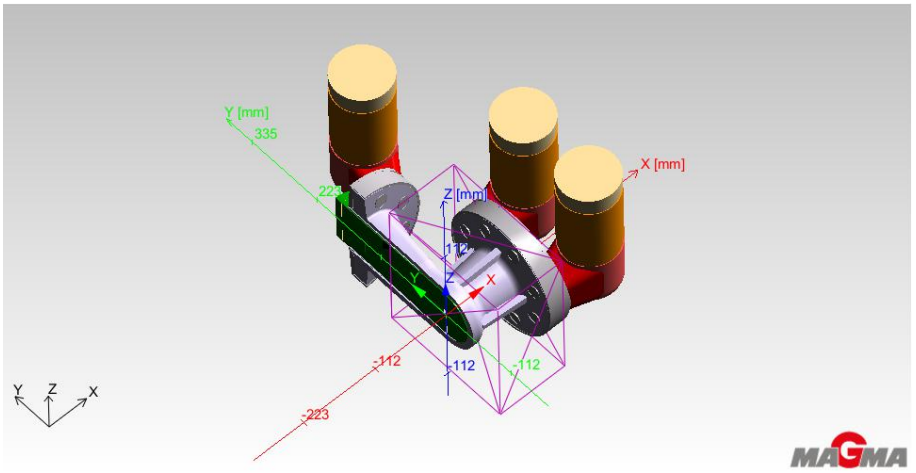

Figure 3.9: Definition of critical area for optimisation investigation

3.3 Results

The results of the numerical investigation are divided into two discussions, firstly the results of the optimisation are presented after which the results from the final simulation is presented where the discussion is focussed on porosity but also touches on other relevant defects.

3.3.1 Optimisation for porosity

The search and convergence history for the four objectives is shown in Figure 3.10. Sufficient simulations are performed to set up a correlation matrix as in Figure 3.11, which shows the correlation between each objective and parameter. Some interesting conclusion can be made from the results:

Initial temperature: A very strong negative correlation ($R^2 = -0.84$) is established between the average microporosity in the critical area i.e. a decrease in temperature will lead to a decrease in average microporosity. This means that the temperature of the melt must be as low as possible without the melt entering the mushy zone during filling. This implies the lowering of the heat energy input into the melt, which will require a lower heat dissipation rate (i.e. the denominator in the Ny criterion). There is also a moderate negative correlation between the maximum value of macroporosity and the initial temperature.

Machining thickness and taper angles (MT, SP and R): The machining thickness and taper angle in the flow and spindle sections have strong positive correlation, up to $R^2 = 0.74$, for the various porosity objectives. The most interesting and unintuitive result lies in the geometry parameter R, which determines the wall thickness and draft angle in the spindle section. The result states that an increase in R, i.e. a small draft angle and minimum wall thickness is preferred in the spindle section, while a thicker wall thickness is preferred in the flow section. There are two possible explanations for this result. The feeding distance from the feeder on the spindle section to the critical area is much longer compared to the feeding distance from the feeders on the flow section to the critical area. This will result in the feeding to the critical section being dominated by the feeder on the flow section flanges. The second explanation comes from the definition of the critical area as seen in Figure 3.9. The critical area encloses the entire flow section and only partially on the spindle section. This again will result in the feeding section feeder dominating the algorithm. The dominance of the flow section feeders is confirmed visually in Figure 3.12 where the solidification time clearly shows the flow section

solidifying later than the spindle section due to the proximity of feeders.

Rib geometry: The rib parameters have very little effect on any of the objectives. It is not clear whether the ribs have been added to the investigation valve for quality purposes, however, from the numerical results it can be concluded that the ribs will only increase the cross-sectional area moment of inertia, and thus strengthen the valve to some extent. The question must be asked whether the added complexity to the core is justified by the added benefit of the ribs. It should also be noted that the ribs could have some effect on the porosity but is simply overshadowed by the other parameters.

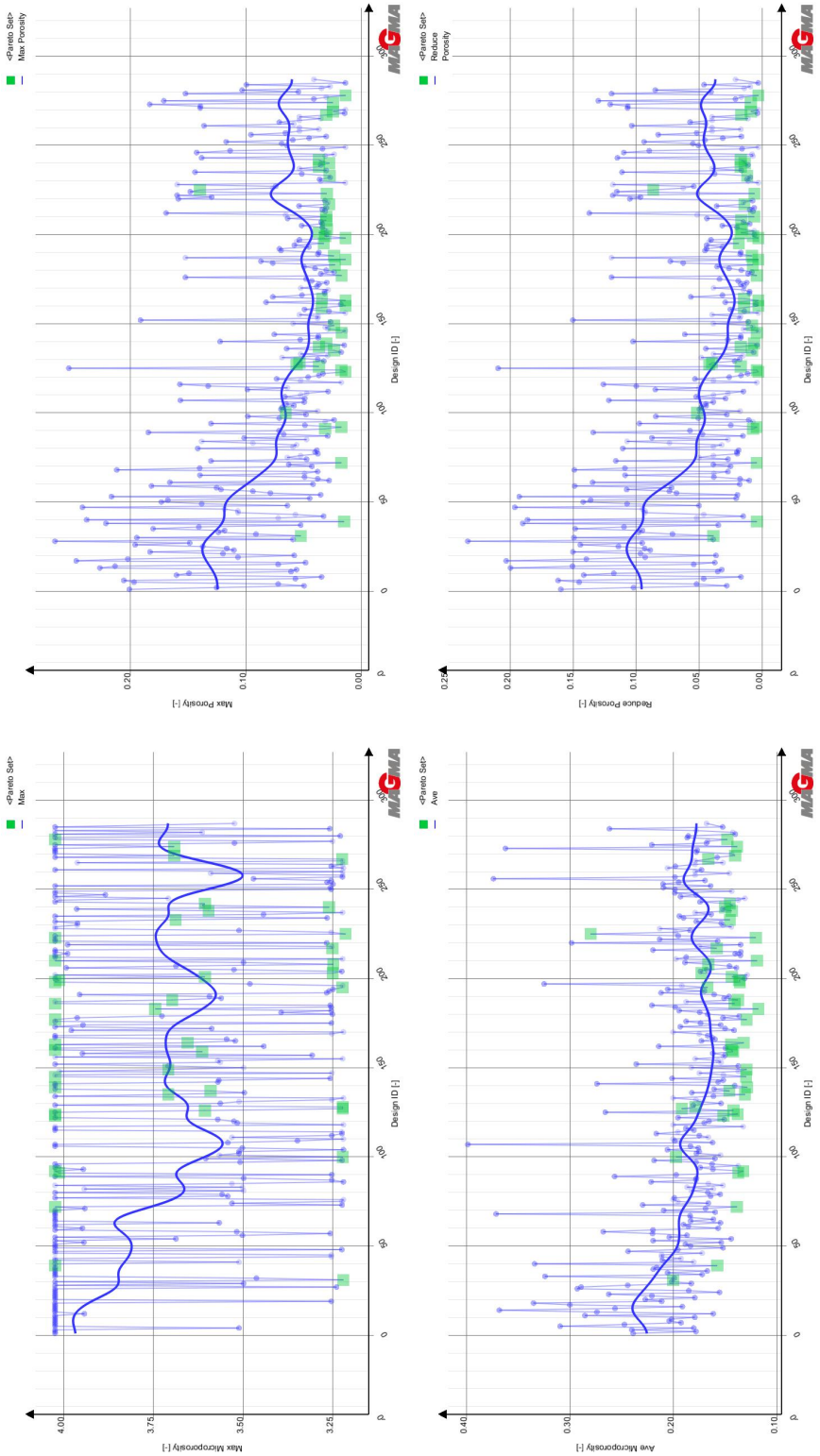

Figure 3.10: Convergence history of different objectives for optimisation

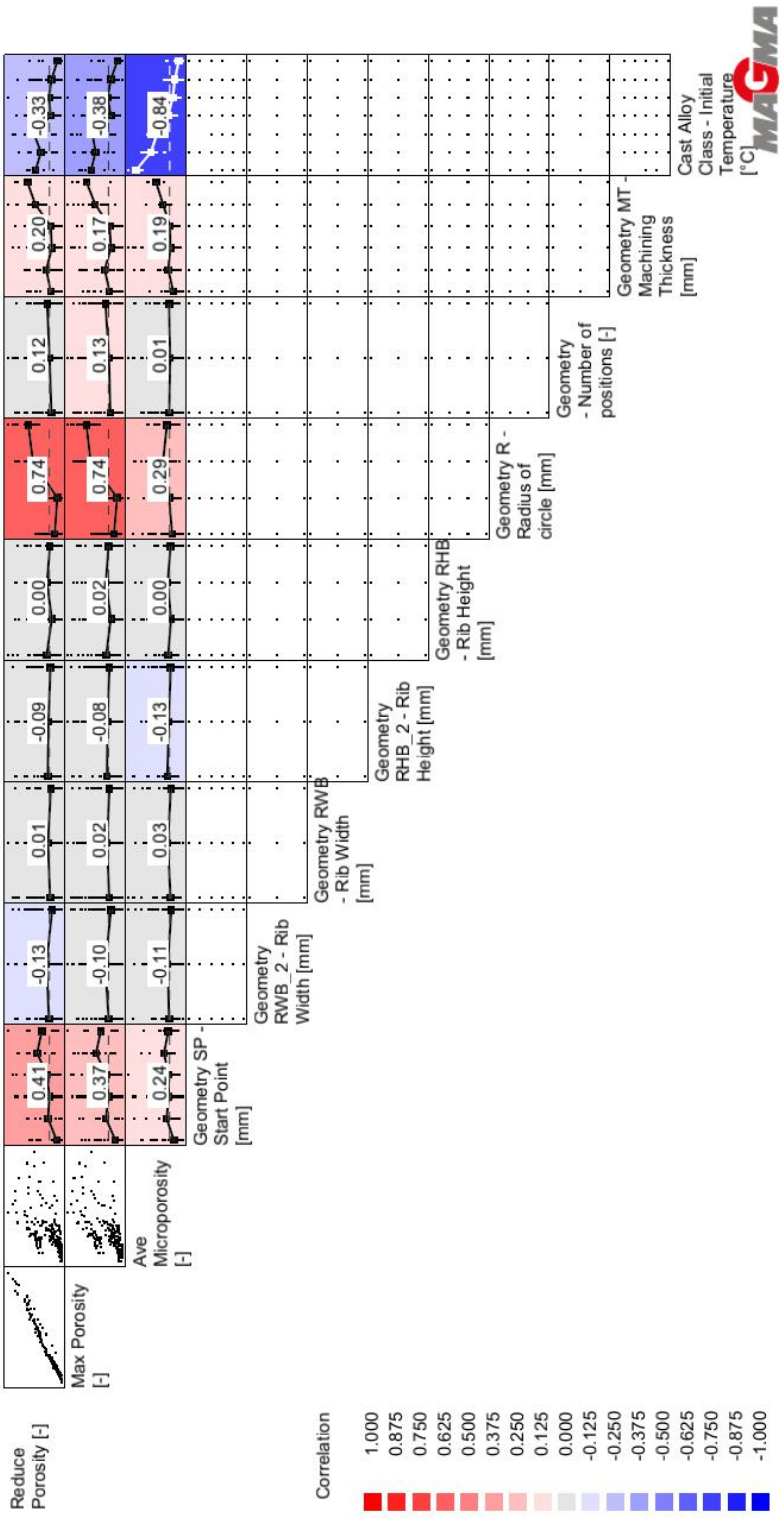

Figure 3.11: Correlation matrix for optimisation parameters

Figure 3.12: Solidification time distribution in valve

3.3.2 Porosity results

The most important parameters relevant to the porosity of the valve body has been identified, the next step is to investigate the actual porosity results. Magmasoft© distinguishes between micro- and macroporosity in the results. The macroporosity distribution is given quantitatively and is calculated from the solution of Equations 3.1 - 3.3. The optimised result, shown in Figure 3.13, has almost no porosity in the critical area of the valve.

The microporosity distribution is given qualitatively, as shown in Figure 3.15. The microporosity results are derived from the Niyama criterion as described in Section 2 which is shown in Figure 3.14. Clearly, there is a high risk of microporosity (Figure 3.15) in the middle of the valve's walls where solidification fronts approach each other swiftly from the wall.

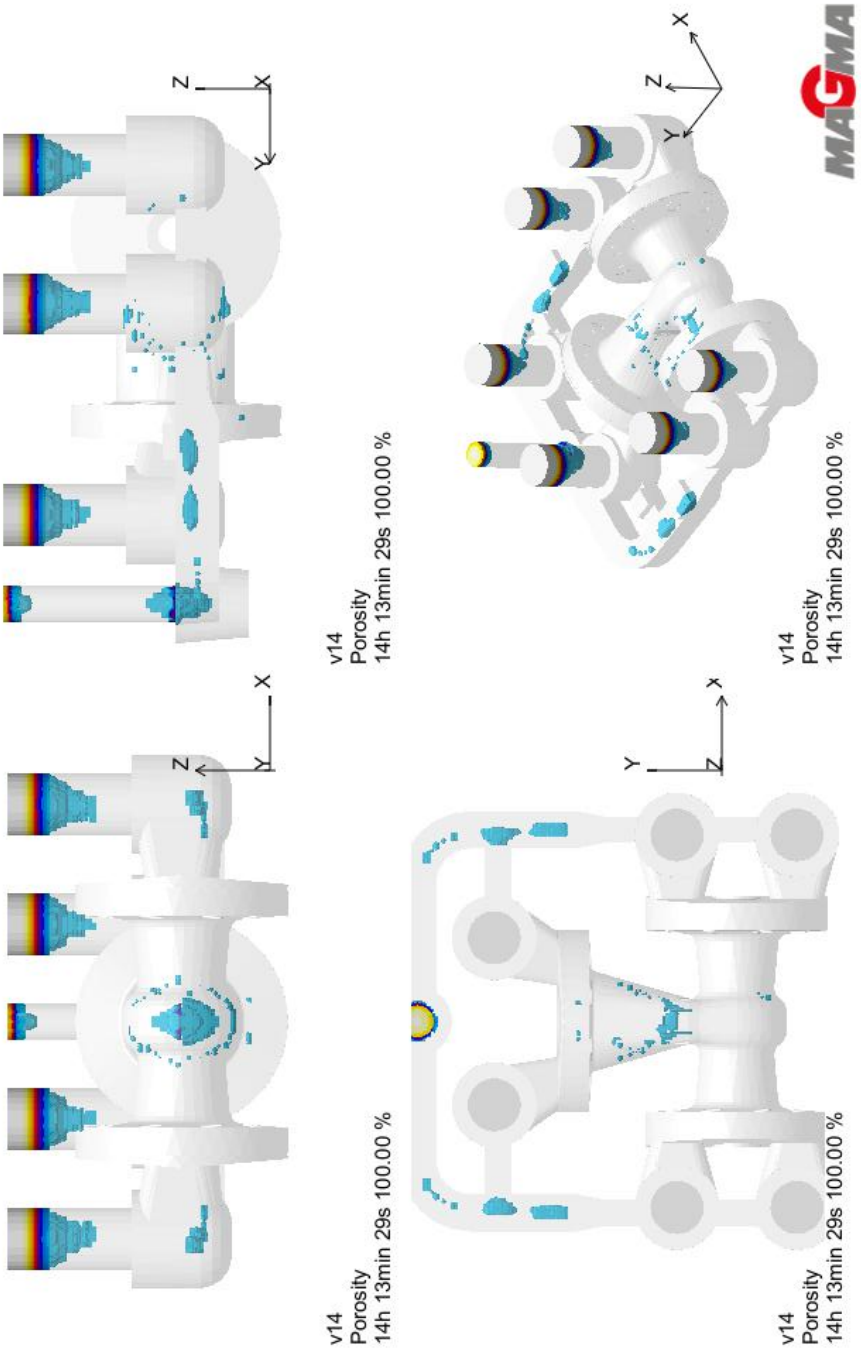

Figure 3.13: Predicted macro porosity distribution

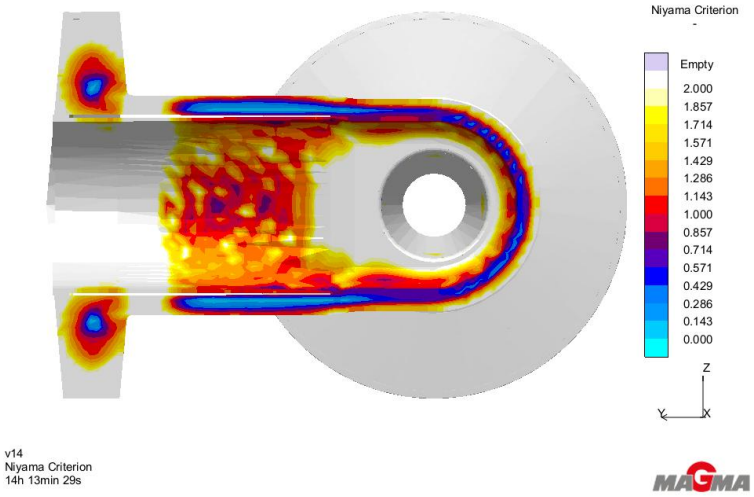

Figure 3.14: Niyama criterion results for simulation

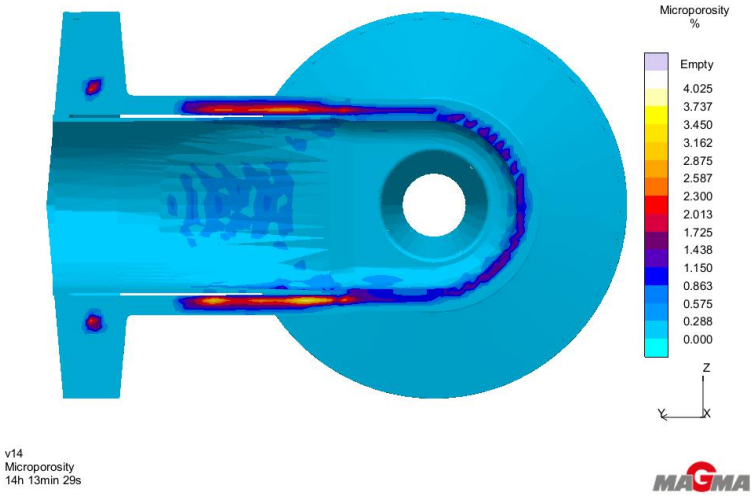

Figure 3.15: Predicted areas of high risk for microporosity

3.3.3 Other defects

A full filling, solidification and stress simulation is performed after the optimal geometry is identified with details as in Table 3.5. Castings have an inherent risk for other defects as well, which might appear as shrinkage defects during an experimental investigation. Some of these possible defects are discussed in the following.

Table 3.5: Details of stress and filling simulation

Parameter	Description
Mesh details	
Mesh size	3 mm
No. of element	854 568
Simulation details	
Filling time	10 sec
Filling temp	1500 °C
Cooling time	14 h
Simulation time	78 h

Inclusions: Inclusions in the final product, whether primary or secondary, can have similar detrimental effects on part performance as with porosity. In practice, it remains difficult and cost-intensive to remove al primary inclusions from the melt, and secondary inclusions can still enter the part from the filling process. An effort is made to capture these inclusions during filling in the runner system as Magmasoft© has the capabilities to simulate the flow and final location of such inclusions. Figure 3.16 shows how most inclusions are trapped in the runner system although some inclusions still manage to enter the part.

Hot tear and cold crack risks: Thermal and solidification shrinkage can cause stress to build in the casting. Cold cracks and hot tears can form when the stresses reach the tensile strength of the material. If the defect forms during solidification (above the solidus temperature), the defect is termed a hot tear while defects that form after solidification (i.e. during cooling) are termed cold cracks.

For hot tears, the mechanical properties of the material in the mushy zone, just before complete solidification, is critical in the calculation. At this state, very little feeding is possible as the dendrite network is very dense. During this state, the mushy zone can already carry some load, although the material properties in this state are brittle which results in the high risk for hot tears. Magmasoft© calculates the regions of high risk for hot tears by evaluating the strain rate in the mushy zone.

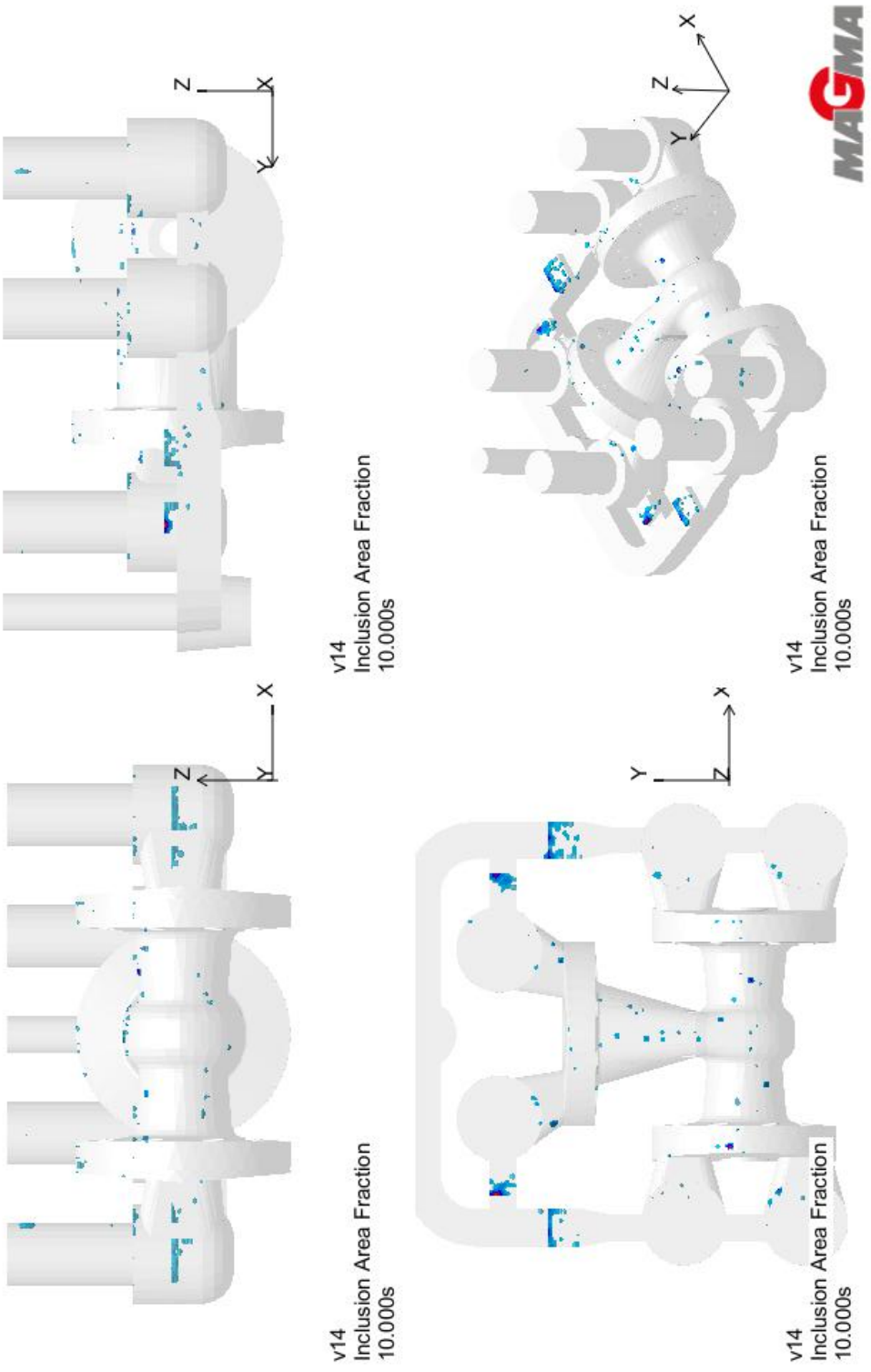

Figure 3.16: Inclusions in casting and runner system after solidification

The risk for cold cracks is calculated by the ratio of the Von Mises stress and the tensile strength at the evaluation temperature. Using the Von Mises stress ensures a positive result.

$$CC = \frac{VonMises\ Stress}{Tensile\ Strenght\ (at\ temperature)} \tag{3.4}$$

The hot tear and cold crack calculation can only identify the regions which has the most risk for cold cracks or hot tears but it cannot conclusively say whether the defects will actually form. Figures 3.17 and 3.18 shows the regions of most risk for hot tears and cold cracks respectively. These regions can be inspected after casting to ensure the part is sound. The residual stress in the casting before machining and heat treatment is also shown in Figure 3.19.

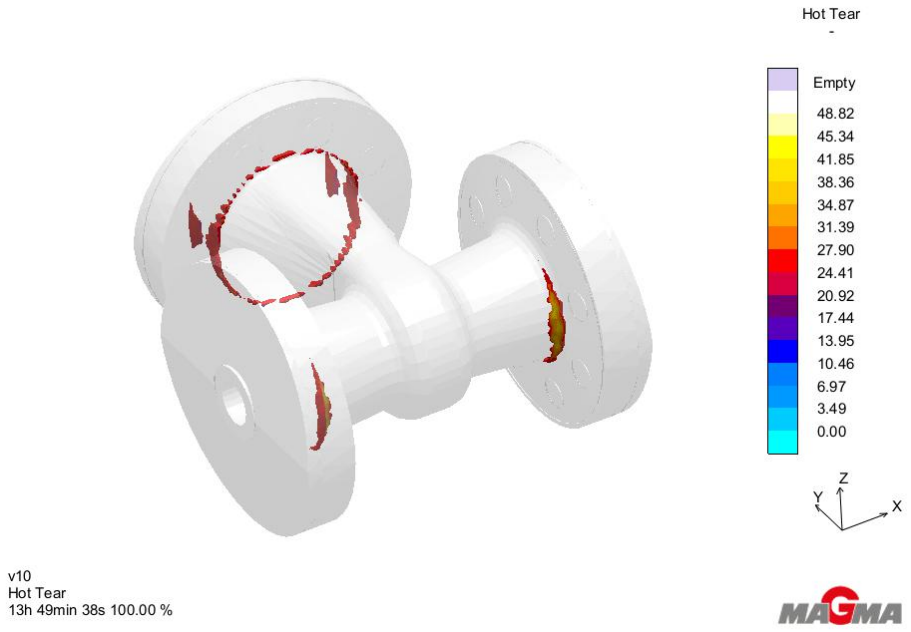

Figure 3.17: Predicted high risk areas for hot tears

3.4 Final Design Manufacturing

The optimised design was presented to China Academy of Manufacturing Science and Technology for trial production who manufactured the mould and

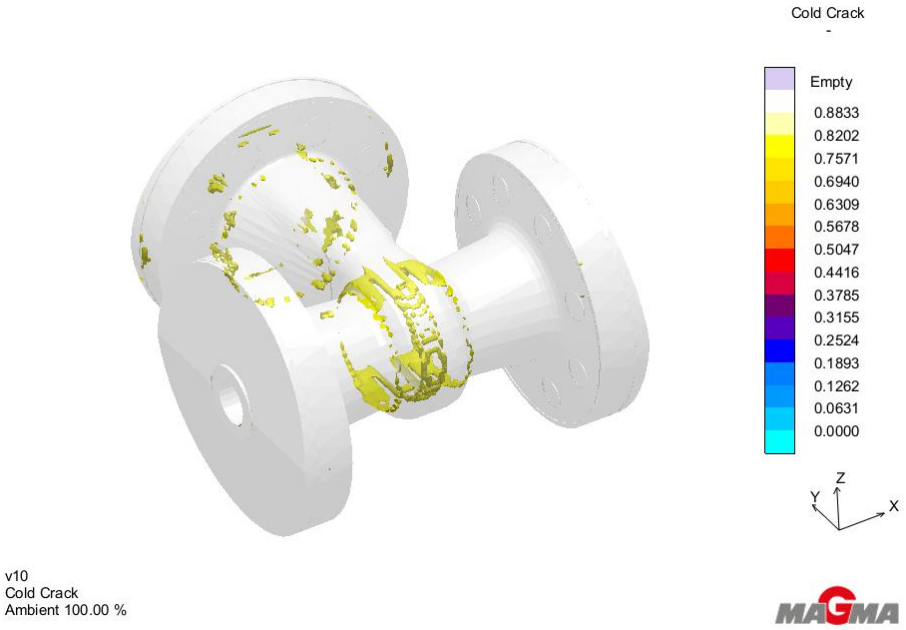

Figure 3.18: Predicted high risk areas for cold cracks

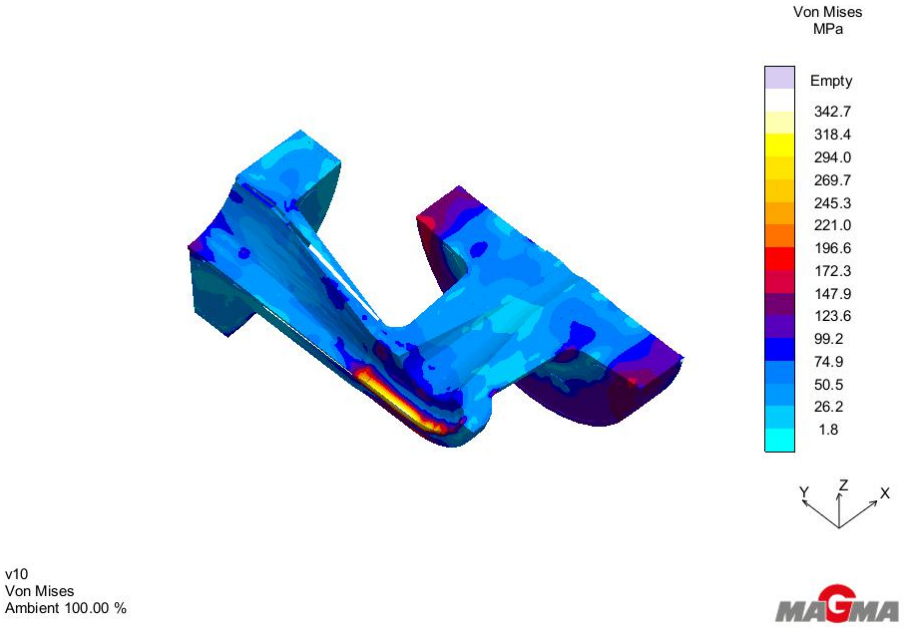

Figure 3.19: Predicted residual stress in valve after cooling

core (Figure 3.20) and cast the valve (Figure 3.21). The mould and core was manufactured by machining a preset sand block into the desired shape rather than using the traditional pattern making process. The valve will be investi-

gated for standard compliance in future work.

Figure 3.20: Photo of mould and core from China Academy of Machinery Science and Technology

Figure 3.21: Photo of optimised valve body from China Academy of Machinery and Technology

3.5 Limitations in the use of numerical optimisation

As with any numerical approach to design, a certain number of limitations exists. The use of commercial software limits the user to the solving algorithm(s), discretisation techniques, meshing methods as well as optimisation algorithm(s) to name a few.

In this study, a number of simplifications/assumptions is made that could influence the final results:

The heat transfer from the mould to the atmosphere can not be specified explicitly in the software used. This can influence the rate of cooling and

solidification, as well as the directional nature of the solidification process. From the Niyama criterion discussed in Chapter 2, this assumption can have an effect on the microporosity results.

The optimisation process utilises a multi-objective objective optimisation process such as described in (**?**), however no mention is given in the software as to which algorithm is used and thus the user is not aware of the limitation of the algorithm. For example, the user can not conclusively state that an optimal design or set of designs has been reached as the algorithm could have converged to a local minima rather than the global minima.

The computational costs of solidification simulations is high, especially for pouring simulation. This study only considered the solidification process in the optimisation and it was assumed that the casting was filled completely at a uniform temperature before solidification starts. This assumption will also influence the solidification pattern as well the the solidification rate.

Chapter 4

EXPERIMENTAL INVESTIGATION

Currently, quality inspection of cast components is performed using traditional two-dimensional radiographic methods. The advancement of technologies such as computed tomography and scanning electron microscopy allows for more detailed examination of cast components. These technologies are used in this chapter with the following aims:

- Investigate the viability of using computed tomography and scanning electron microscopy for quality inspections.
- Investigate the required quality for ASTM-E2868 (2013), ASTM-A216 (2014) and ASME-B16.34 (2013) compliance.

Keeping with the valve theme, a 2-inch gate valve body, acquired off the shelf, is used for the experimental investigation. The valve body, which complies with all the standards and regulations relevant to this study, is shown in Figure 4.1. A technical drawing of the valve is given in Appendix C.

The investigation is divided into two categories, namely a computed tomography (CT) investigation for macro-scale features and a scanning electron microscopy (SEM) investigation for microscale features and elemental composition verification of the material.

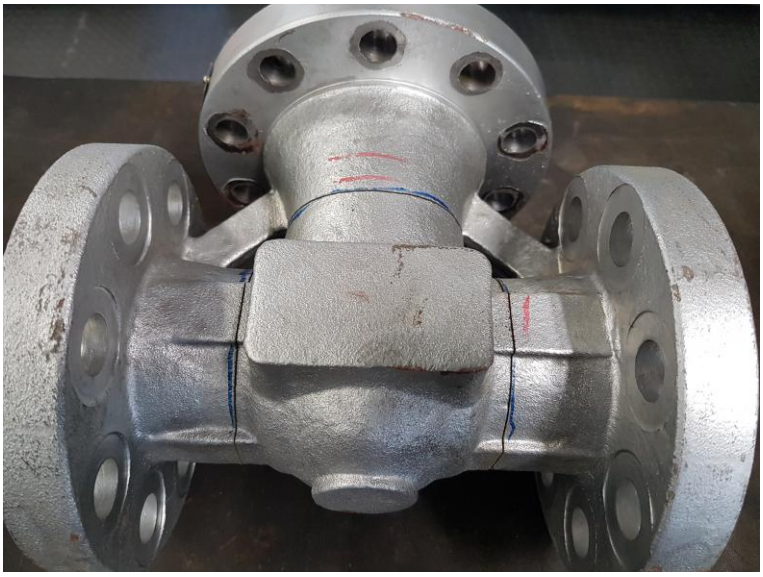

Figure 4.1: Valve body used in experimental investigation

4.1 Computed Tomography (CT) Investigation

The CT scanner available to this research, as described in Table 4.1, does not have the power to scan the valve body in full due to the steel density and thickness in some sections. Ideally, the entire valve body should be investigated, although, in accordance with ASME-B16.34 (2013), only the critical sections have to be verified for compliance. The required areas are shown in Figure 4.2. This allowed for a destructive testing strategy, focussing on the critical sections.

Table 4.1: Micro-CT system specifications (Du Plessis *et al.*, 2016*a*)

Technical specification	**Details**
Voltage	10 kV to 240 kV
Current	5 μA to 3000 μA
Best voxel size	5 μm
Beam angle	30 °
Sample restrictions	
Weight	50 kg
Height	320 mm
Width	300 mm
Wall thickness (steel)	10 mm

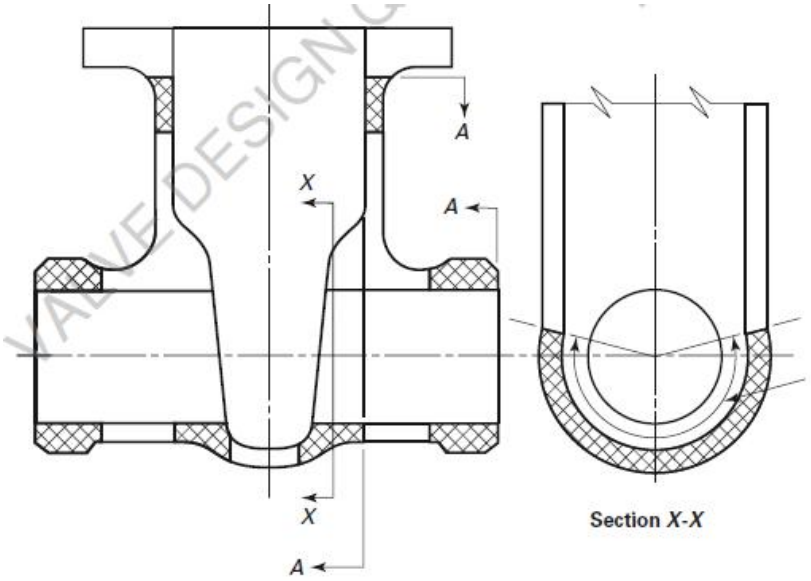

Figure 4.2: Required testing areas for gate valve body (ASME-B16.34, 2013)

4.1.1 CT strategy

The valve was machined using a wire cutting process and examined with computed tomography in accordance to ASTM-E1570 (2017). The image rendering of the scanned section, termed valve *halfneck*, from here on, is shown in Figure 4.3. The main objective of the CT scans is to successfully identify macro-scale defects. The SEM investigation (Section 4.2.2) required further cutting of the valve body. These smaller parts were also scanned with CT for more accurate results. The smaller sections are shown in Figure 4.4.

CT scans were performed at the Stellenbosch CT Facility, using a General Electric V|TomeX L240 system. Visualization and analysis was performed in MyVGL 3.0. The scan details for the three scans is provided in table 4.1. For the scanning of the smaller parts, it was possible to enable detector shift to minimise artifacts.

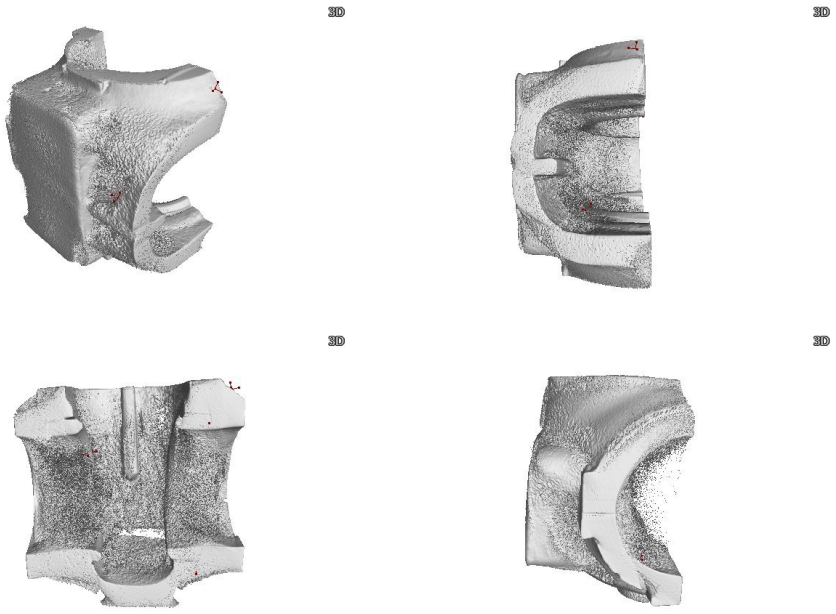

Figure 4.3: CT scan of half neck - Part 01

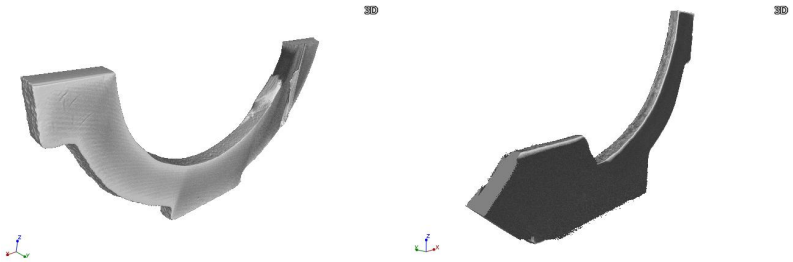

Figure 4.4: Smaller parts (Detail 1 left and Detail 2 right) scanned for more detailed analysis

4.1.2 Summary of CT results

The focus of this study is shrinkage porosity, although other common defects are shown for the sake of completeness. As defined in ASTM-E2868 (2013), when a hot tear or cold crack is not on the surface, it might appear similar to shrinkage porosity and may be assumed to be shrinkage porosity. It is not possible to conclusively classify all of the defects shown below. All defects that can't be conclusively classified is treated as shrinkage defects as they are most severe, according to ASME-B16.34 (2013).

Table 4.2: CT settings used in porosity investigation

Setting [Unit]	Large cut out	Detail 1	Detail 2
Voltage [V]	220	200	200
Ampere [μ A]	250	100	100
Copper beam filtration [mm]	1.5	-	-
Voxel size [μ m]	140	55	55

Shrinkage porosity defects: Although the *halfneck* scan was still too thick for the capabilities of the CT scanner and thus showed some measurement noise, called artifacts in CT as described in du Plessis *et al.* (2017), as seen in Figure 4.3, a substantial number of shrinkage porosity defects were found. A select few are shown in Figures 4.5 - 4.7. The results show varying size and distribution of the defects. The distinct line of defect-like features in Figure 4.5 can be either microporosity or artifacts from the scanning process. Defects found in the smaller samples of Figure 4.4 is shown in Figures 4.8 - 4.10. Some of these defects are too small to be seen in the *halfneck* scan, although it will be shown in Section 5 that the data from the *halfneck* is sufficient to determine standard compliance.

Other defects: A large sand or slag inclusion was found in the part as shown in Figure 4.11. This feature was analysed using SEM for species analysis, and is discussed further in Section 4.2.2. Figure 4.11 shows an example of gas porosity. Very few gas pores were found in the part, which indicated good melt treatment during the casting process.

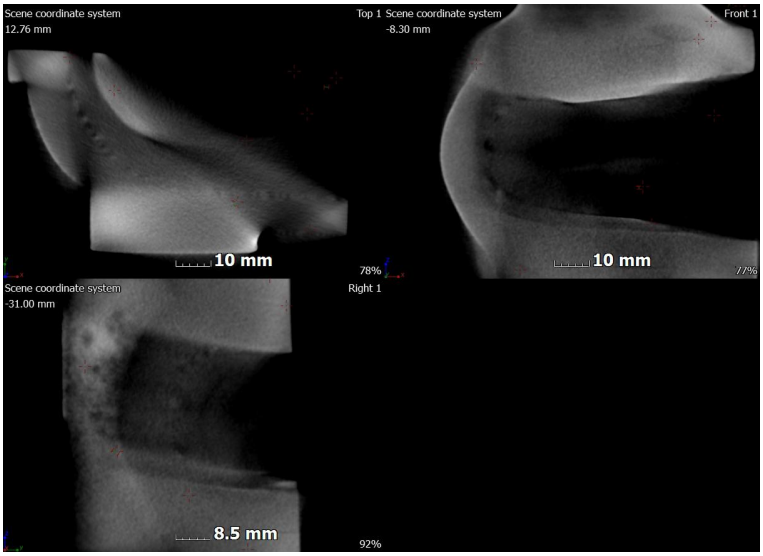

Figure 4.5: Halfneck scan showing macroporosity and possible microporosity

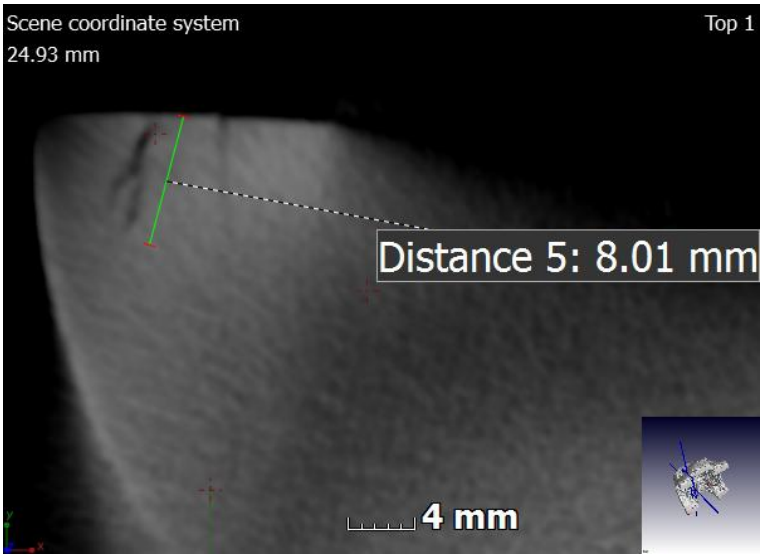

Figure 4.6: Hafneck scan showing large shrinkage porosity defect

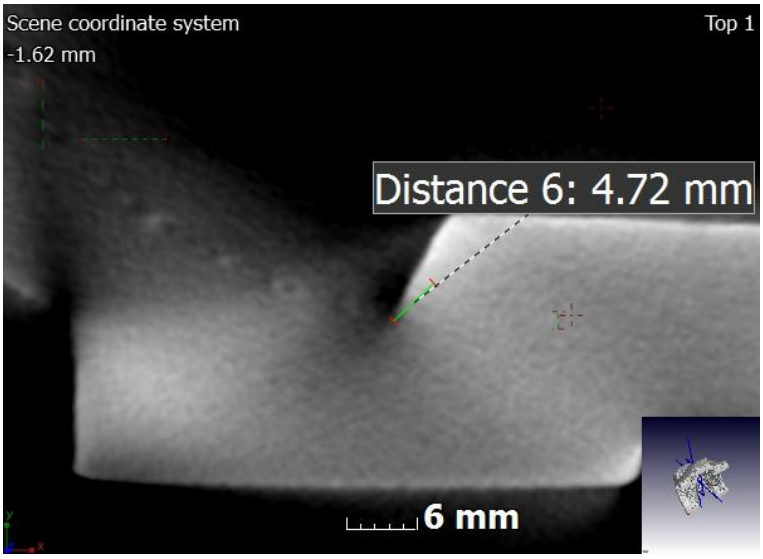

Figure 4.7: Halfneck scan showing large porosity and possible microporosity or artifacts

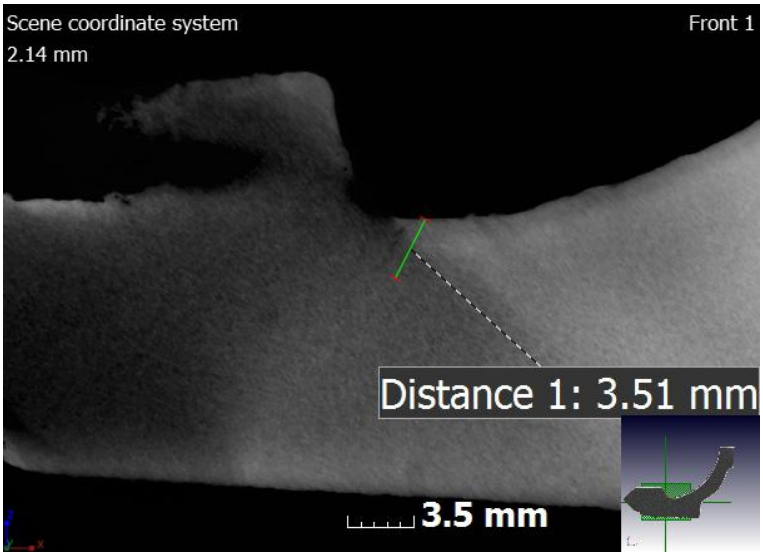

Figure 4.8: Smaller sample 1 scan showing defect in improved details

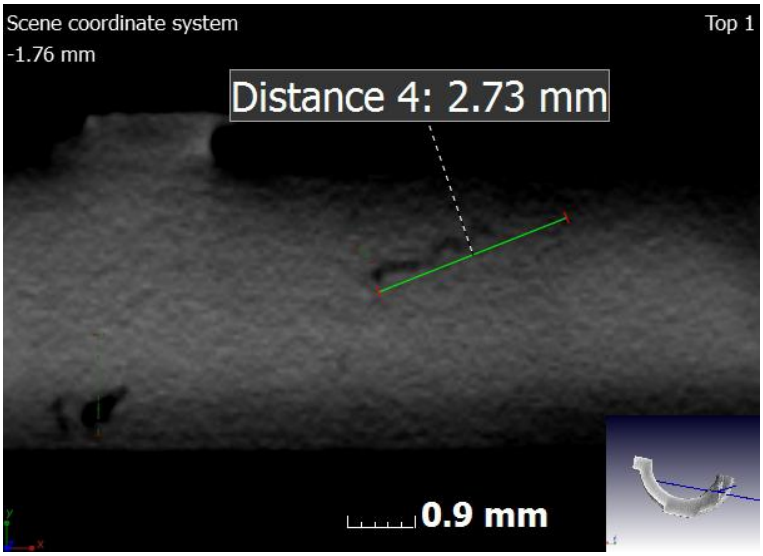

Figure 4.9: Smaller sample 2 scan showing defect in improved details

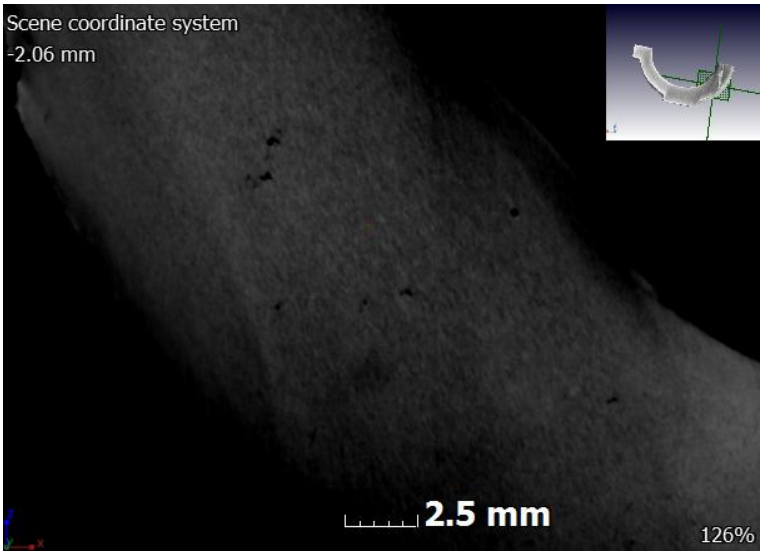

Figure 4.10: Smaller sample 2 scan showing high density of shrinkage pores

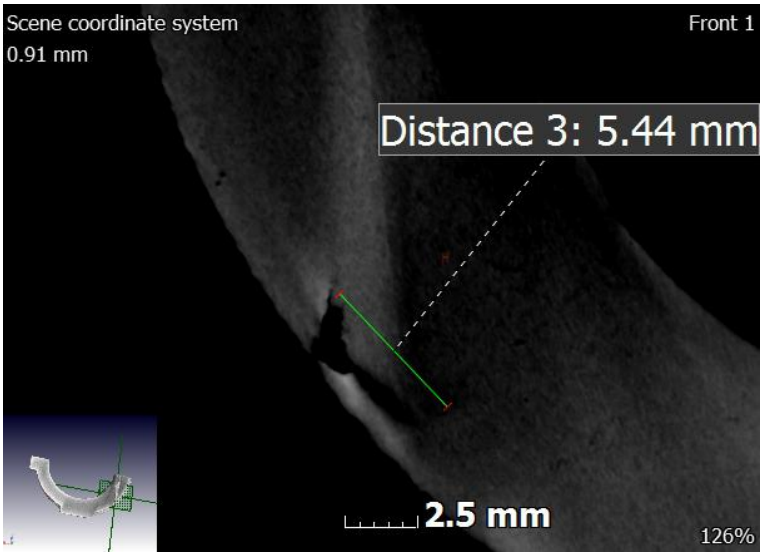

Figure 4.11: Smaller sample 2 scan showing a large sand inclusion

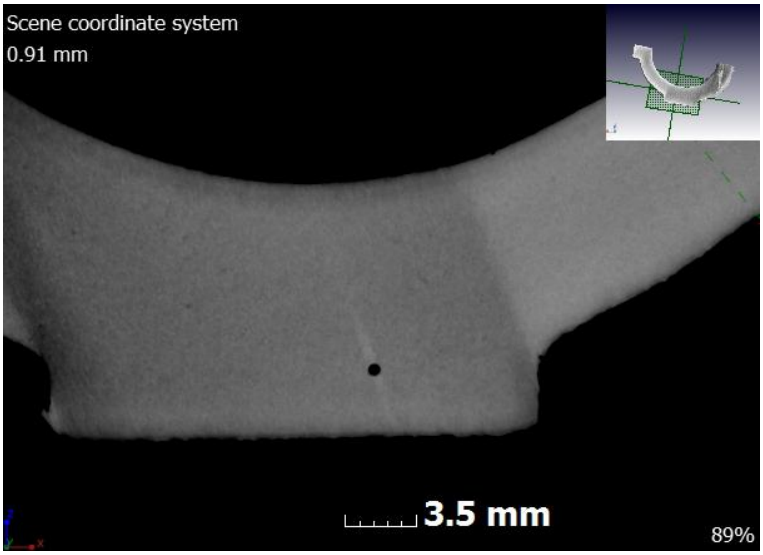

Figure 4.12: Smaller sample 2 scan showing clear gas pore

4.2 Scanning Electron Microscopy Investigation

The samples shown in Figure 4.4, was analysed with a Zeiss © Merlin scanning electron microscope. The details of the SEM equipment can be seen in ZEISS

(2017). The samples were cut using a wire-cutter in an effort to not disturb the microstructure by means of heat treatment as a result of elevated temperature exposure in the machining effected zone.

4.2.1 SEM strategy

The capabilities of SEM, discussed in Chapter 2, allows investigation of the microstructure features such as phases and grain structure, elemental composition analysis (for identification of microsegregation) and the identification of microporosity. With this in mind, two types of samples are analysed. Polished samples (from critical areas in the valve) to investigate the microstructural features of the material with an emphasis on microporosity as well as an elemental analysis of the material, and an unpolished sample to investigate the elemental composition of the large inclusion found in the valve.

4.2.2 Summary of SEM results

Microporosity on polished sample: Figures 4.13 and 4.14 shows the size and distribution of typical microporosity found in the valve. The detrimental effect of microporosity on mechanical performance is discussed in Chapter 2. This result only confirms the presence of microporosity in the valve, but the extent of the subsequent affect on performance cannot be concluded from these SEM images. It should also be noted that these images do not mean non-compliance with the standards as only macro-scale defects are considered in the standards.

Inclusion analysis: SEM allows for elemental analysis, and is used to identify the inclusion type. Table 4.3 shows the elemental analysis for three sampling points on the inclusion. The elemental analysis distribution of the inclusion is shown in Figures 4.17 and 4.18. From this data, it can be concluded that the inclusion is quartz, most likely from the sand mould used during filling.

Steel elemental analysis: An elemental analysis was performed at various sampling points on the polished samples. It is found that all the species are in the range prescribed by ASTM-A216 (2014), except for carbon which is

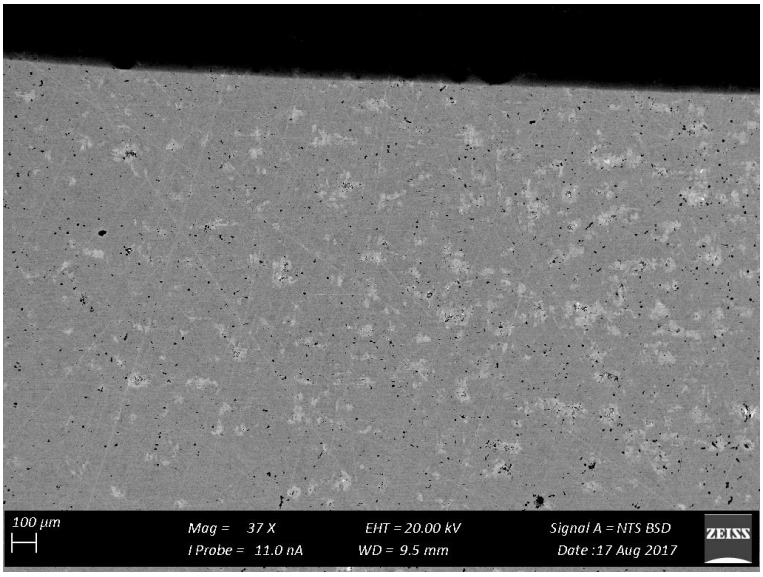

Figure 4.13: Microporosity size and distribution on large scale

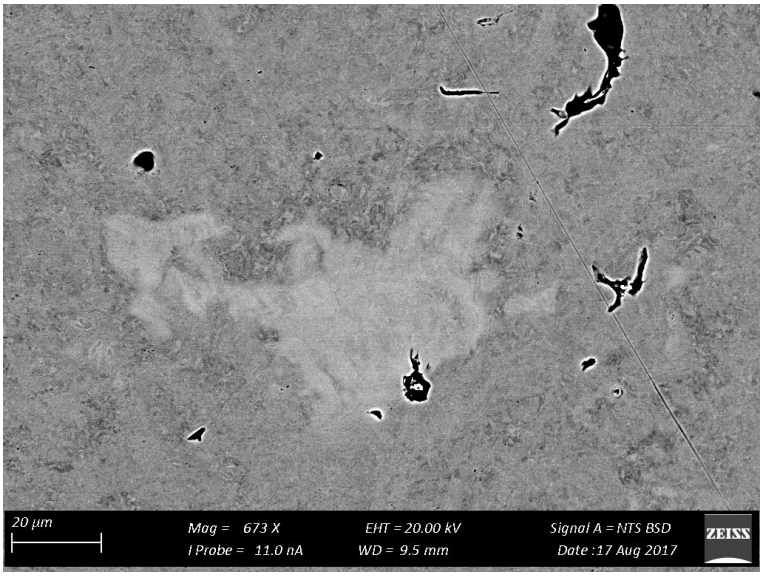

Figure 4.14: Microporosity size and distribution on small scale

consistently higher than the prescribed value. The deviation is not conclusive evidence for non-compliance with the standard. SEM elemental analysis loses accuracy for lighter elements. Typically, any elemental analysis results for elements lighter than sodium cannot be trusted as accurate. Another possible reason for the consistent high carbon readings can be the polishing process which uses a carbon-based paste. An effort is made to remove the carbon paste

after polishing although some residue could still be present on the sample. The elemental analysis results for all the sampling points (polished and unpolished samples) is added in Appendix D

Table 4.3: Elemental analysis of inclusion depicted in Figure 4.17

	Analysis area number		
Element	55 (Figure 4.15)	56 (Figure 4.16)	57 (Figure 4.16)
C	36.86	29.97	33.95
O	26.08	47.39	4.81
Na	0.74	0.53	
Mg	1.60	4.92	7.31
Al	1.81	2.13	0.96
Si	4.46	5.58	2.09
Ca	26.22	1.79	4.81
Fe	94.95	26.22	4.81

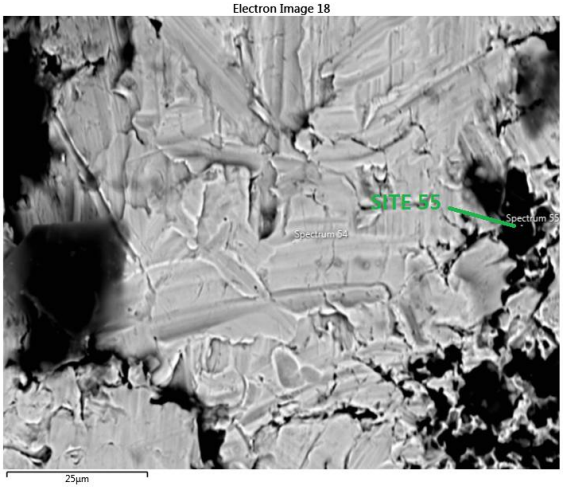

Figure 4.15: Magnified area 1 of inclusion defect

4.3 Comments On The Use of CT and SEM for Quality Inspection

From the results above it can be concluded that CT and SEM are viable methods for quality inspection. As with all experimental investigations, the

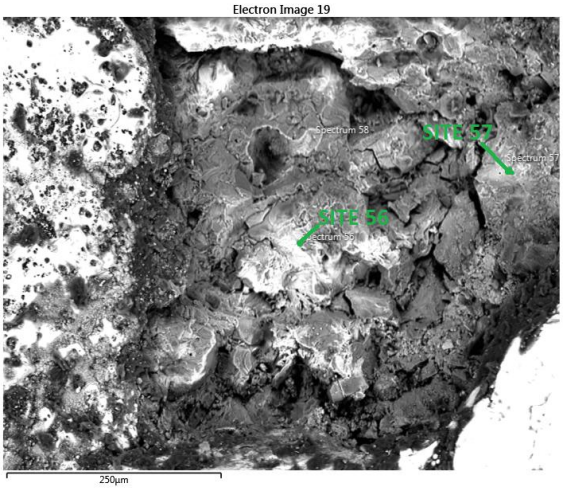

Figure 4.16: Magnified area 2 of inclusion defect

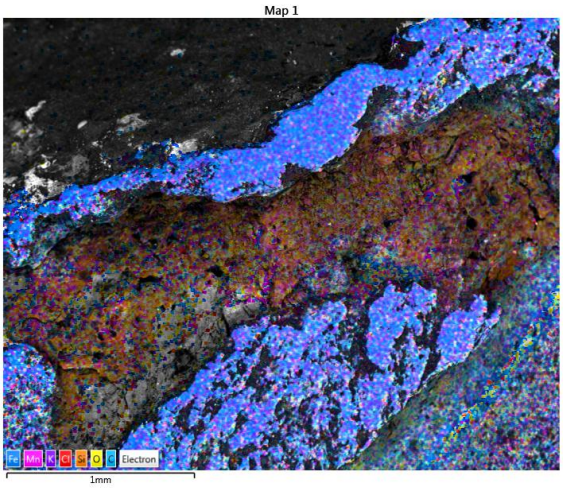

Figure 4.17: SEM image of combined elemental analysis of inclusion

results should be interpreted with the limitations of the testing methods in mind.

For CT, a lack of penetrating power can lead to artifacts in the results which might appear as defects. Experienced CT operators are able to distinguish between artifacts and actual defects.

For SEM, the sample preparation process is key. Insufficient polishing will result in unclear images and will complicate interpretation. Another limitation of SEM is the compositional analysis functionality. During the investigation,

it became clear that the carbon readings are unrealistic which is explained by the loss in accuracy for elements lighter than sodium. External factors such as sample preparation can also influence the compositional analysis.

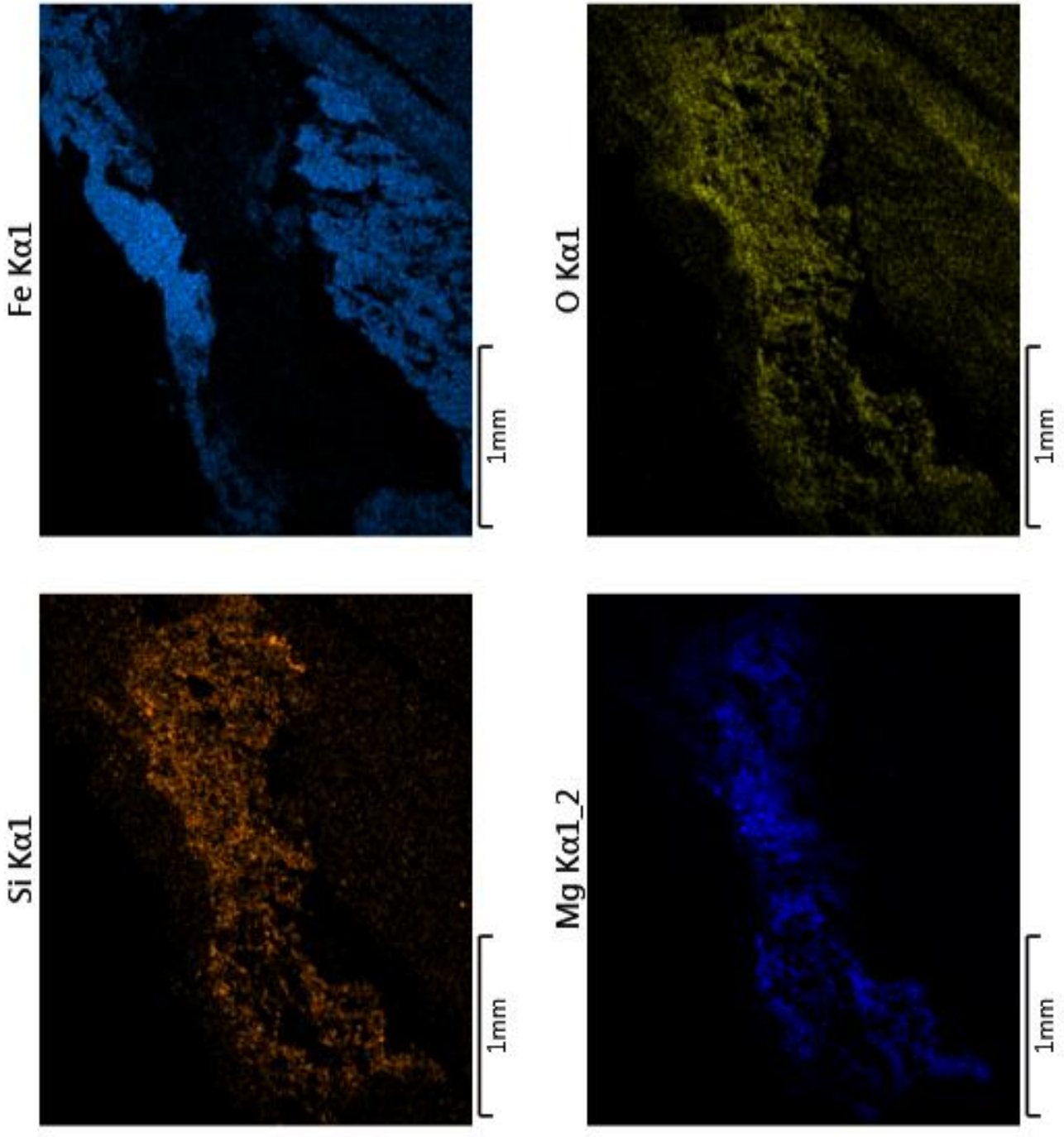

Figure 4.18: Individual elemental analysis of inclusion

Chapter 5

ALTERNATIVE COMPLIANCE TESTING PROPOSAL

The aim of this section is to present an alternative compliance testing procedure to the current procedure given in ASTM-E2868 (2013) which is described in Section 2. The alternative strategy aims to be more objective and to reduce ambiguity in classifying the severity of casting defects.

5.1 Critique of Current Compliance Testing

The current standard compliance testing procedure has the following disadvantages:

- The procedure requires a subjective comparison of production radiographs with a set of reference images or radiographs.
- The operator might need to pro-rate the radiographs if the scale of the production radiographs is different to the reference images.
- There is no connection between the severity levels and the subsequent effect on performance (Blair *et al.*, 2008).
- The reference images are provided with different severity levels but no clear distinction between the different severity levels.

These disadvantages can be visualized in Figures 5.1 - 5.5 where the defects for each severity level of defect category C_a are identified and marked. In a reproducibility and repeatability study of 128 radiographs, Carlson *et al.* (2001) found that only severity level 1 and 5 could be unanimously agreed to. For severity level 2, 3 and 4 the variance levels were up to 2 levels for the 95% confidence interval.

There is little difference between the average defect length for all 5 severity levels as seen in Figure 5.1. The average length was normalised using the width (177.8 [mm]), height (127 [mm]) and thickness (assumed 50.8 [mm]), although this does not improve variance between the severity levels.

Table 5.1: Average shrinkage porosity data for 5 severity levels

Severity	**Ave defect [mm]**	**Ave normalized:**		
		Thickness	**Width**	**Height**
1	5.33	0.10	0.03	0.04
2	6.40	0.13	0.04	0.05
3	5.25	0.10	0.03	0.04
4	7.07	0.14	0.04	0.06
5	8.55	0.17	0.05	0.07

Figure 5.1: Category C_a severity level 1 defects identified and measured

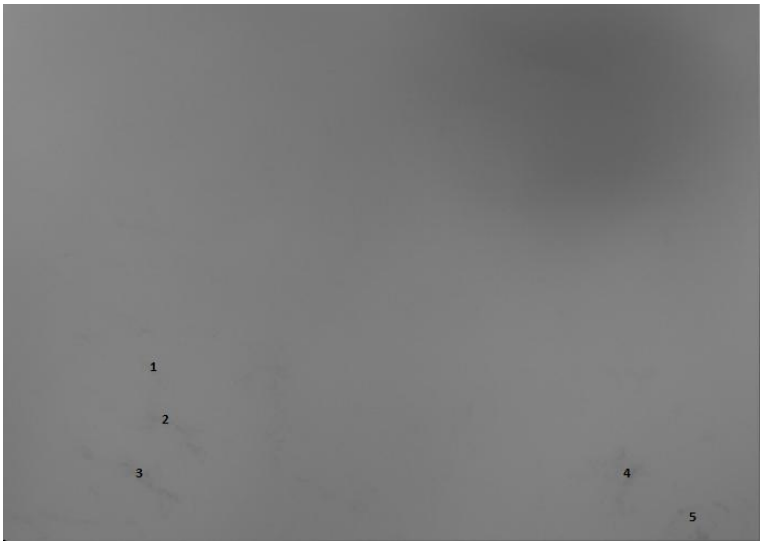

Figure 5.2: Category C_a severity level 2 defects identified and measured

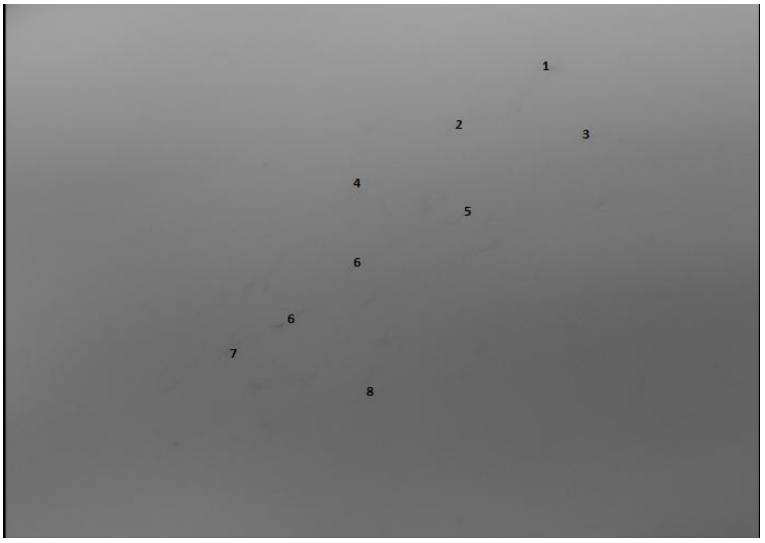

Figure 5.3: Category C_a severity level 3 defects identified and measured

5.2 Alternative Methods for Standard Compliance Testing

Clearly, the size and distribution (i.e. number of defects), must be considered when performing compliance testing. In the following, two alternative testing methods are proposed for compliance testing. Both methods aim to create objective testing procedures and parameters.

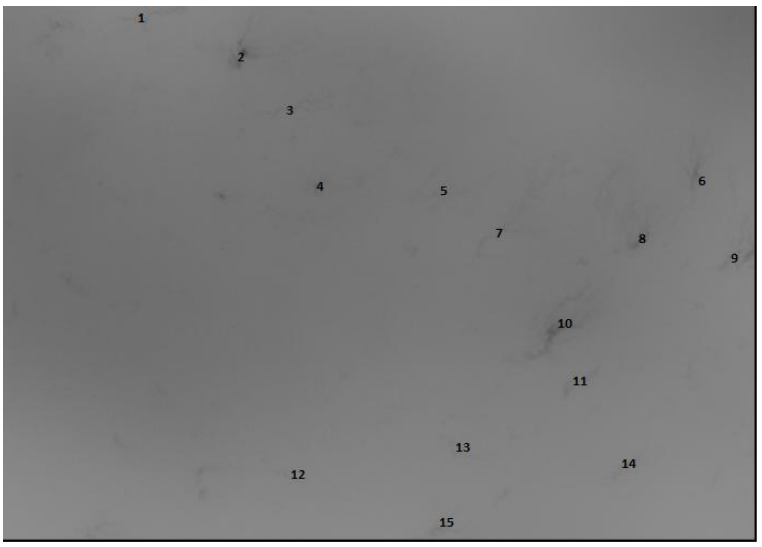

Figure 5.4: Category C_a severity level 4 defects identified and measured

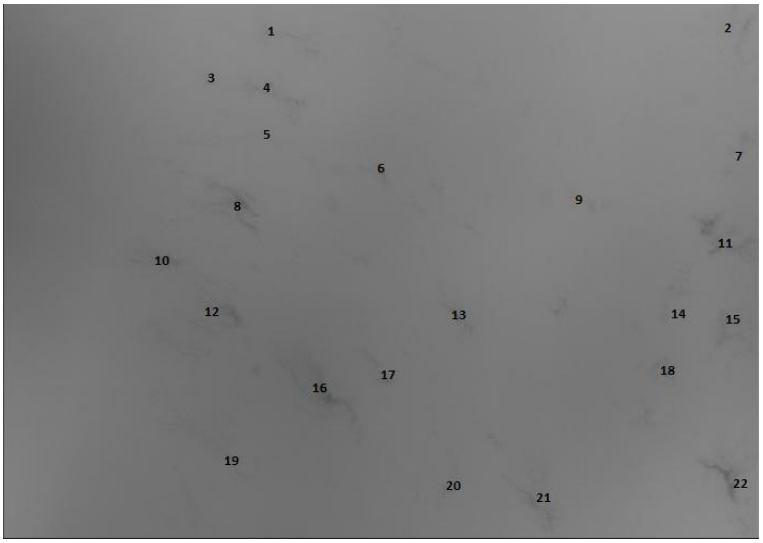

Figure 5.5: Category C_a severity level 5 defects identified and measured

5.2.1 Normalising ASTM-E2868 defects

The total length of all the defects for each severity level is normalised with the same parameters (width, height, thickness) and summarized in Figure 5.6. Using such normalised values for standard compliance has been proposed by Blair *et al.* (2008) in which he considered the defect size and direction. This method allows the manufacturer and client to objectively agree on the acceptance criteria in terms of the normalisation parameter (probably some feature-length

such as a minimum wall thickness) and the corresponding normalised value.

5.2.2 Using crack density parameters

An alternative method is to use a crack density parameter to normalize the defects. Various crack density formulas are available in the literature. The most common, described in Kachanov (1992), takes the form:

$$CD_A = \frac{1}{A}\sum l_i^2 \tag{5.1}$$

$$CD_V = \frac{1}{V}\sum l_i^3 \tag{5.2}$$

Where

CD	is the the crack density,
A	is the total area of part or of the section being investigated,
V	is the total volume of the part or the section being investigated, and
i	is the instance member, i.e. each defects is measured individually and added to the

Assuming a thickness of 50.8 [mm] for the reference images in ASTM-E2868 (2013), the area and volume crack densities are calculated and presented in Table 5.2. These values provide objective threshold values for severity level classification.

Using computed tomography scans and (objective) defect identification software, which is available commercially, the number of defects, size of defects and the applicable normalising volume can be identified with minimum human interaction in the process. In this way, standard compliance can become reliable, repeatable and automated.

5.2.3 Limitations

The crack density method described above does have a few limitations. Parts that require compliance testing can not be machined for testing as in this study, thus the CT system used must have sufficient penetrating power to scan the

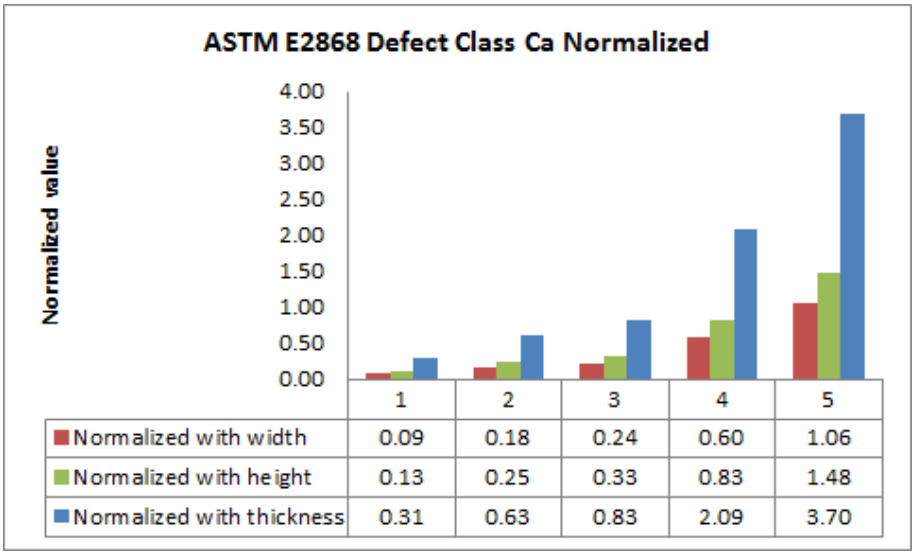

Figure 5.6: Total crack length normalised for ASTM-E2868 (2013) category C_a severity levels

Table 5.2: Area and volume crack density for ASTM-E2868 (2013) category C_a severity levels

Severity	Area Crack Density	Volume Crack Density
1	2.83	0.45
2	11.34	3.57
3	19.53	8.07
4	124.40	129.79
5	1931.31	724.08

whole part. Such systems requires significant capital input. Using CT for compliance testing will also require expertise for operating CT systems and investigation time will be significantly longer compared to traditional x-ray testing.

Furthermore, there is no data available for the effect of crack density on the mechanical and material properties. Before a complete compliance testing method can be proposed, a number of tests will be required to correlate crack density to part performance.

Chapter 6

CONCLUSION

This study approached the general problem of casting quality with a strong focus on shrinkage porosity. The study aimed to develop new techniques to improve the design and manufacturing process as well as improving standard compliance testing procedures. This is completed using various technologies, such as numerical simulation of the casting process, computed tomography, and scanning electron microscopy.

6.1 Discussion of Results

The results of this study can be classified into two distinct categories, in line with the research objectives. The first is a numerical simulation study which involves optimisation for minimum porosity. The second is an experimental porosity investigation using computed tomography and scanning electron microscopy.

6.1.1 Numerical prediction of porosity

The numerical investigation was used to optimise the process and geometrical parameters of a valve body. This was conducted using commercially available software, Magmasoft©. This allowed for the virtual casting of over 350 different configurations, which would be impossible using traditional casting trial methods. From this, the parameters which have the most influence on the

quality of the valve were identified. These results were not always intuitive, further proving the importance of using simulation technology in the design of casting processes for complex-shaped components. The design space was kept relatively small due to the unknown details of the optimisation algorithms and no conclusion can be made regarding local or optimal minima in the design space. The success of the optimisation studies lies in the correlation of various parameters and their respective effect on porosity.

From the optimisation investigation, an optimal valve body was designed, which complies with the minimum geometrical requirements set out in the relevant standards. The trial valve body was then cast at the China Academy of Machinery Science and Technology, and will be tested for porosity levels in future work using the testing methods proposed in this study. It was concluded that the use of simulation technology is essential in the design process as it can drastically reduce casting trials, improve process efficiency and, most importantly, improve part quality, however certain limitations exists in the use of these simulations. Most notably, the limitations of using commercial software was identified. A need exists for open source software for solidification processes in which the user has complete control over the boundary conditions, solving algorithms, descretisation methods ext. The academic industry will benefit most from such open source software.

6.1.2 Use of CT and SEM for quality investigation

Traditional radiography is still the accepted standard for quality inspection of cast parts in industry. This study investigated the use of alternative inspection methods, such as computed tomography (CT) and scanning electron microscopy (SEM). CT was used to investigate the quality of a commercially available valve on a macro scale, while the microscale porosity was investigated using SEM. The focus was to successfully identify and classify shrinkage porosity defects, although an effort is made to comment on other defects found in the valve.

The CT equipment available to this study required a destructive testing strategy. The valve was cut using a wire cutter in an effort not to disturb the

micro-scale features. A critical section of the valve was then scanned using CT and various defects were found throughout the part.

CT allowed for three-dimensional visualisation of defects and the exact location and direction of the defects, which is not possible using traditional two-dimensional radiography. The investigation also showed some possible pitfalls in using CT scanning, such as artifacts created by the scanning process which might have a similar appearance as defects however, CT is used in the newly proposed standard compliance testing method in which a crack density parameter is used. The limitations of CT lies in the large capital expenditure of the systems, the expertise required in using these systems as well as interpreting the results. Most significantly, most commercially available CT systems does not have the required penetrating power to scan large, dense parts and is more suited to lighter materials such as aluminium and bio-materials. The compliance testing methodology proposed in this work can be readily be applied to any casting material.

The SEM results showed a clear presence of microporosity in the valve which could have a detrimental effect on the in-service performance of the valve. Various references were cited which prove the was provided which proves the danger of microporosity. SEM was also used to investigate the chemical composition of the valve material which has to conform to the relevant standard. Most elements are found to be in the correct range with the notable exception of carbon. Further investigation found that SEM struggles for accuracy with lighter elements such as carbon. It is also found that the carbon reading could be affected by the sample polishing process which uses a carbon-based polish. SEM, like CT, also requires large capital investment and expertise in operation. If no elemental analysis is required, other forms om microscopy such as light optical microscopy (LOM) can be more suited for porosity investigations.

6.2 Discussion of Objectives

The study had two main objectives:

- Develop a strategy to minimize porosity in castings using simulation technology.
- Develop an alternative strategy for testing ASME-B16.34 compliance.

In Chapter 2, the detrimental effect of porosity on part performance was investigated. From this, it was clear that porosity should be considered in the design stage, and thus a clear need exists for a design strategy to minimise the porosity. This was completed in the study by designing a valve body that complies with the relevant standards in geometrical terms after which a numerical simulation procedure was used to minimise porosity (Chapter 3). Various literature was cited in which simulation technology was used to successfully predict shrinkage porosity defects in cast components in an effort to build confidence in the technology. The first objective is thus successfully completed.

For the third objective, two alternative strategies were proposed. The first, proposed by Blair *et al.* (2008), still uses traditional radiography, normalises the defect with some characteristic length and is then classified for severity using the normalised values. The second strategy prosed the use of CT to identify defects. A crack density can then be calculated and compared with the crack density of the defects in the relevant standard. Both these proposed strategies are more objective than the current methods used in industry.

6.3 Future Work

This study is the first in a planned series of studies for casting quality improvement. This study achieved all of its set objectives and certain new research objectives for future work were identified in the process.

6.3.1 Validation of numerical simulation

There is still some doubt as to the accuracy and reliability of numerical modelling of the solidification process. Future work will focus on complete verification of numerical modelling in an controlled environment. Alternative

solidification modelling software will be considered in which the user will have more control over the simulation parameters. Furthermore, simulation results can be exported to strengths analysis software (traditional FEM) to validate fatigue and tensile test results.

6.3.2 Correlation of crack density to performance

This study proposed a new compliance testing strategy in which a crack density parameter is used. Currently there is no correlation between crack density and the subsequent effect on performance of the material. Future work can focus on creating testing methods to establish such a correlation. The work can also investigate other crack density formulations to determine the suitability of the various formulations. Once the correlations have been established, the compliance testing of critical components will be based on actual data rather than subjective images.

List of References

Amirirad, Y., Afkar, A. and Wisweh, L. (2014). Analysis of porosity-induced stress intensity factors for the evaluation of inline-computer tomography scans of cast parts. *The International Journal of Advanced Manufacturing Technology*, vol. 74, no. 9-12, pp. 1469–1485. ISSN 0268-3768.

API-600 (2015). API-600: Steel Gate Valves - Flanged and Butt-Welding Ends, Bolted Bonnets.

ASME-B16.10 (2017). ASME B16.10: Face to Face and End to End Dimensions of Valves.

ASME-B16.34 (2013). ASME-B16.34: Valves - Flanged , Threaded , and Welding End.

ASTM-A216 (2014). ASTM-A216: Standard Specification for Steel Castings, Carbon, Suitable for Fusion Welding, for High-Temperature Service.

ASTM-E1570 (2017). ASTM E1570-11: Standard Practice For Computed Tomographic (CT) Examination.

ASTM-E2868 (2013). ASTM E2868: Standard Digital Reference Images for Steel Castings up to 2 in (50.8mm) in Thickness.

ASTM-E446-14 (2013). ASTM E446-14: Standard Reference Radiographs for Steel Castings Up to 2 in. (50.8 mm) in Thickness.

Bednarz, P. and Szwedowicz, J. (2015). Engineering Approach for Low-Cycle Fatigue Assessment of Porous Alloys. *Journal of Engineering for Gas Turbines and Power*, vol. 138, no. 4, p. 042101. ISSN 0742-4795.

Blair, M., Monroe, R., Hardin, R. and Beckermann, C. (2008). A New Standard for Radiographic Acceptance Criteria for Steel Castings. In: *62nd SFSA Technical and Operating Conference*. Chicago.

Bossi, R.H. and Georgeson, G.E. (1992). Computed Tomography Analysis of Castings. Tech. Rep., Boeing Aerospace and Electronics, Seattle.

Campbell, J. (2003). *Castings*. 2nd edn. Elsevier, Oxford. ISBN 978-0-7506-4790-8.

Carlson, K. and Beckermann, C. (2009*a*). Authors' Reply to Discussion of "Prediction of Shrinkage Pore Volume Fraction Using a Dimensionless Niyama Criterion". *Metallurgical and Materials Transactions A*, vol. 40, no. 13, pp. 3054–3055. ISSN 1073-5623.

Carlson, K.D. and Beckermann, C. (2008). Use of the Niyama Criterion To Predict Shrinkage-Related Leaks in High-Nickel Steel and Nickel-Based Alloy Castings. In: *62nd SFSA Technical and Operating Conference*, pp. 1–18.

Carlson, K.D. and Beckermann, C. (2009*b*). Prediction of Shrinkage Pore Volume Fraction Using a Dimensionless Niyama Criterion. *Metallurgical and Materials Transactions A*, vol. 40, no. 1, pp. 163–175. ISSN 1073-5623.

Carlson, K.D., Lin, Z., Beckermann, C., Mazurkevich, G. and Schneider, M.C. (2006). Modelling Porosity Formation In Aluminum Alloys. *Modeling of Casting, Welding and Advanced Solidification Processes*, vol. 11, pp. 627–634.

Carlson, K.D., Lin, Z., Hardin, R.A. and Beckermann, C. (2002). Modelling of Porosity Formation and Feeding Flow in Steel Casting. In: *56th SFSA Technical and Operating Conference*. Chicago.

Carlson, K.D., Ou, S., Hardin, R. and Beckermann, C. (2001). Analysis of ASTM X-ray shrinkage ratings for steel castings. *International Journal of Cast Metals Research*, vol. 14, pp. 169–183.

Cormack, A.M. (1973). Reconstruction of densities from their projections, with applications in radiological physics. *Physics in Medicine and Biology*, vol. 18, no. 2, p. 003. ISSN 00319155.

Cupido, L.H., Żak, P.L., Mahomed, N., Lelito, J., Piwowarski, G. and Krajewski, P.K. (2015). Experimental Investigation of Modified Heat Treatment Of AK64-

Type Al-SI-Cu Sand Cast Alloy. *Archives of Metallurgy and Materials*, vol. 60, no. 3, pp. 2397–2402.

Dantzig, J.A. and Rappaz, M. (2009). *Solidification*. EPFL Press. ISBN 978-2-940222-17-9.

du Plessis, A., Broeckhoven, C., Guelpa, A. and le Roux, S.G. (2017 jun). Laboratory x-ray micro-computed tomography: a user guideline for biological samples. *GigaScience*, vol. 6, no. 6, pp. 1–11. ISSN 2047-217X.

Du Plessis, A., Gerhard Le Roux, S. and Guelpa, A. (2016*a*). The CT Scanner Facility at Stellenbosch University: An open access X-ray computed tomography laboratory. *Nuclear Instruments and Methods in Physics Research B*, vol. 384, pp. 42–49.

Du Plessis, A., Le Roux, S.G. and Guelpa, A. (2016*b*). Comparison of medical and industrial X-ray computed tomography for non-destructive testing. *Case Studies in Nondestructive Testing and Evaluation*, vol. 6, pp. 17–25.

Du Plessis, A. and Rossouw, P. (2015). X-ray computed tomography of a titanium aerospace investment casting. *Case Studies in Nondestructive Testing and Evaluation*, vol. 3, pp. 21–26.

Du Plessis, A., Yadroitsava, I., le Roux, S.G., Yadroitsev, I., Fieres, J., Reinhart, C. and Rossouw, P. (2017). Prediction of mechanical performance of Ti6Al4V cast alloy based on microCT-based load simulation. *Journal of Alloys and Compounds*, vol. 724, pp. 267–274. ISSN 09258388.

Gilboy, W.B. (1984). X-and y-Ray Tomography in NDE Applications. *Nuclear Instruments and Methods in Physics Research*, vol. 221, pp. 193–200.

Hardin, R.A. and Beckermann, C. (2007). Effect of Porosity on the Stiffness of Cast Steel. *Metallurgical and Materials Transactions A*, vol. 38, no. 12, pp. 2992–3006. ISSN 1073-5623.

Hardin, R.A. and Beckermann, C. (2009). Prediction of the Fatigue Life of Cast Steel Containing Shrinkage Porosity. *Metallurgical and Materials Transactions A*, vol. 40, no. 3, pp. 581–597. ISSN 1073-5623.

Hardin, R.A. and Beckermann, C. (2012). Integrated design of castings: effect of porosity on mechanical performance. *IOP Conference Series: Materials Science and Engineering*, vol. 33, no. 1, p. 012069. ISSN 1757-899X.

Hardin, R.A. and Beckermann, C. (2013). Effect of Porosity on Deformation, Damage, and Fracture of Cast Steel. *The Minerals, Metals and Materials Society and ASTM International*, vol. 44, no. A, pp. 5316–5331.

Kachanov, M. (1992). Effective Elastic Properties of Cracked Solids: Critical Review of Some Basic Concepts. *Applied Mechanical Reviews*, vol. 45, no. 8.

Li, J., Chen, R., Ma, Y. and Ke, W. (2014). Characterization and Prediction of Microporosity Defect in Sand Cast WE54 Alloy Castings. *Journal of Materials Science & Technology*, vol. 30, pp. 991–997.

MAGMA-GmbH (2017). *Magmasoft© V5.3.1.* MAGMA GmbH, Aachen.

Müller, P., Cantatore, A., Andreasen, J.L., Hiller, J. and De Chiffre, L. (2013). Computed tomography as a tool for tolerance verification of industrial parts. *Procedia CIRP*, vol. 10, pp. 125–132. ISSN 2212-8271.

Niyama, E., Uchida, T. and Morikawa, M. (1982). A method of shrinkage prediction and its application to steel casting practice. *Int. Cast Metals*, vol. 54, pp. 507–516.

Ol'khovik, E. (2015). Study of the Effect of Shrinkage Porosity on Strength Low Carbon Cast Steel. *IOP Conference Series: Materials Science and Engineering*, vol. 91, no. 1, p. 012022. ISSN 1757-8981.

Rzyankina, E., Szeliga, D., Mahomed, N. and Nowotnik, A. (2013). Investigation of the Effect of Solidification Velocity on the Quality of Single Crystal Turbine Blades. *Applied Mechanics and Materials*, vol. 372, pp. 54–61. ISSN 1662-7482.

Sigl, K., Hardin, R., Stephens, R. and Beckermann, C. (2004). Fatigue of 8630 cast steel in the presence of porosity. *International Journal of Cast Metals Research*, vol. 17, no. 3.

Sigworth, G.K. (2009). Discussion of "Prediction of Shrinkage Pore Volume Fraction Using a Dimensionless Niyama Criterion". *Metallurgical and Materials Transactions A*, vol. 40, no. 13, pp. 3051–3053. ISSN 1073-5623.

Stefanescu, D.M. (2005). Computer simulation of shrinkage related defects in metal castings âĂŞ a review. *International Journal of Cast Metals Research*, vol. 18, no. 3, pp. 129–143. ISSN 1364-0461.

Susan, D.F., Crenshaw, T.B. and Gearhart, J.S. (2015). The Effects of Casting Porosity on the Tensile Behavior of Investment Cast 17-4PH Stainless Steel. *Journal of Materials Engineering and Performance*, vol. 24, no. 8, pp. 2917–2924. ISSN 1059-9495.

Tavakoli, R. (2014). On the prediction of shrinkage defects by thermal criterion functions. *The International Journal of Advanced Manufacturing Technology*, vol. 74, no. 1-4, pp. 569–579. ISSN 0268-3768.

Versteeg, H. and Malalasekera, W. (2007). *An Introduction to Computational Fluid Dynamics: The Finite Volume Method*. 2nd edn. Pearson, London. ISBN 978-0-13-127498-3.

ZEISS (2017). Zeiss Merlin SEM.
Available at: `https://www.zeiss.com/microscopy`

APPENDIX A - BEST FIT CODE

```
close all
clear all

avePor = [0.104 0.101 0.101 0.128 0.097 0.134 0.095 0.185
0.146 0.213 0.117 0.148 0.185 0.139 0.187 0.076 0.096 0.085
0.093 0.099 0.122 0.117 0.121 0.144 0.129];

maxPor = [0.432 0.208 0.256 0.297 0.185 0.275 0.201 0.363
0.587 0.326 0.250 0.415 0.538 0.507 0.551 0.160 0.254 0.148
0.225 0.182 0.300 0.262 0.205 0.288 0.280];

elasticMod = [137 149 143 138 153 145 141 135 87 135 136
113 77 120 87 166 111 145 142 143 125 151 155 142 148];

fatigueCycles = [1365 79908 24320 851275 29023 216516
4053800 57566 10812 37089 113503 15419 6042 160 15868
1681018 4392 1342218 13013 249752 41066 769074 40896 333025
7456];

createFits(avePor, elasticMod, maxPor, fatigueCycles)
```

```
function [fitresult, gof] = createFits1(avePor, elasticMod,
maxPor, fatigueCycles)
%CREATEFITS1(AVEPOR,ELASTICMOD,MAXPOR,FATIGUECYCLES)
%  Create fits.
%
%  Data for 'ModulusWithAvePor' fit:
%      X Input : avePor
%      Y Output: elasticMod
%  Data for 'ModulusWithMaxPor' fit:
%      X Input : maxPor
%      Y Output: elasticMod
%  Data for 'FatigueWithAvePor' fit:
%      X Input : avePor
%      Y Output: fatigueCycles
%  Data for 'FatigueWithMaxPor' fit:
%      X Input : maxPor
%      Y Output: fatigueCycles
%  Output:
%      fitresult : a cell-array of fit objects representing
the fits.
%      gof : structure array with goodness-of fit info.
%
%  See also FIT, CFIT, SFIT.

%  Auto-generated by MATLAB on 04-Oct-2017 22:40:02

%% Initialization.

% Initialize arrays to store fits and goodness-of-fit.
fitresult = cell( 4, 1 );
gof = struct( 'sse', cell( 4, 1 ), ...
    'rsquare', [], 'dfe', [], 'adjrsquare', [], 'rmse', []
);

%% Fit: 'ModulusWithAvePor'.
[xData, yData] = prepareCurveData( avePor, elasticMod );

% Set up fittype and options.
ft = fittype( 'poly1' );

% Fit model to data.
[fitresult{1}, gof(1)] = fit( xData, yData, ft );

% Plot fit with data.
```

```
figure( 'Name', 'ModulusWithAvePor' );
h = plot( fitresult{1}, xData, yData );
legend( h, 'elasticMod vs. avePor', 'ModulusWithAvePor',
'Location', 'NorthEast' );
% Label axes
xlabel("avePor")
ylabel("elasticMod")
grid off

%% Fit: 'ModulusWithMaxPor'.
[xData, yData] = prepareCurveData( maxPor, elasticMod );

% Set up fittype and options.
ft = fittype( 'poly1' );

% Fit model to data.
[fitresult{2}, gof(2)] = fit( xData, yData, ft,
'Normalize', 'on' );

% Plot fit with data.
figure( 'Name', 'ModulusWithMaxPor' );
h = plot( fitresult{2}, xData, yData );
legend( h, 'elasticMod vs. maxPor', 'ModulusWithMaxPor',
'Location', 'NorthEast' );
% Label axes
xlabel("maxPor")
ylabel("elasticMod")
grid off

%% Fit: 'FatigueWithAvePor'.
[xData, yData] = prepareCurveData( avePor, fatigueCycles );

% Set up fittype and options.
ft = fittype( 'power2' );
opts = fitoptions( 'Method', 'NonlinearLeastSquares' );
opts.Display = 'Off';
opts.StartPoint = [0.00494721689060877 -8.76832815683479 -
2667620.44433941];

% Fit model to data.
[fitresult{3}, gof(3)] = fit( xData, yData, ft, opts );

% Plot fit with data.
figure( 'Name', 'FatigueWithAvePor' );
```

APPENDIX B - MESH INDEPENDENCE DATA

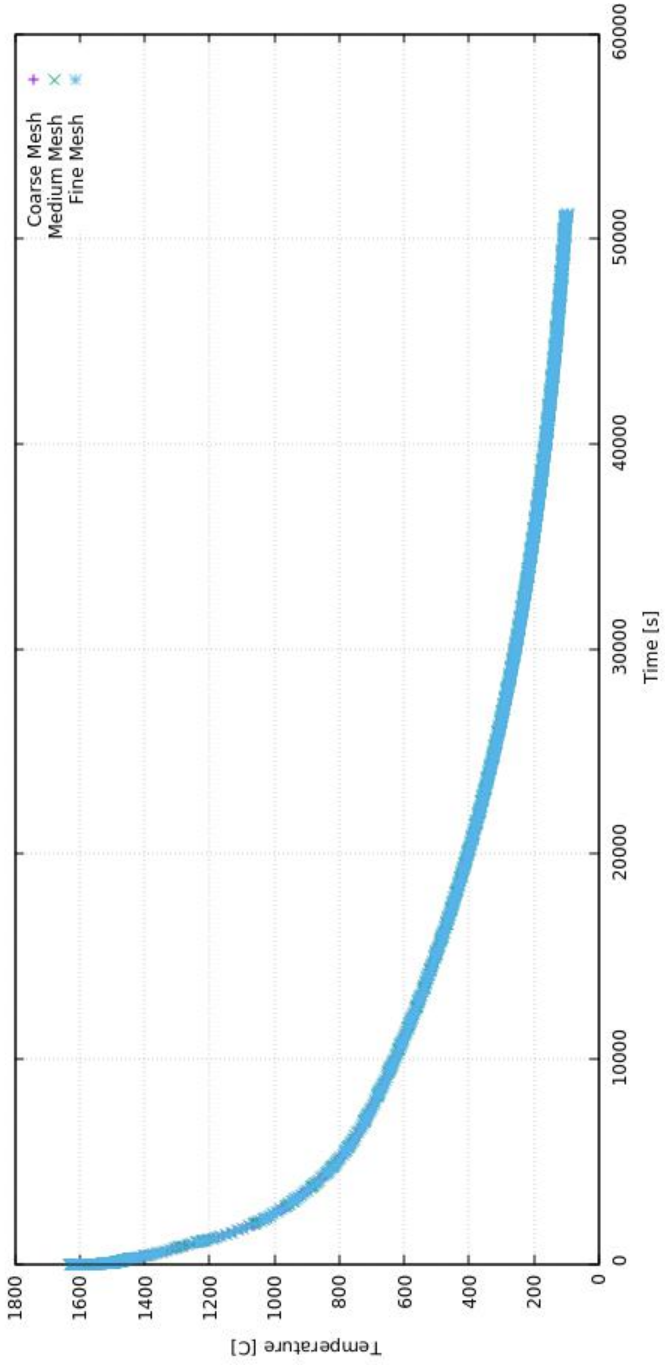

Figure B.1: Mean temperature in casting history for three successively refined meshes

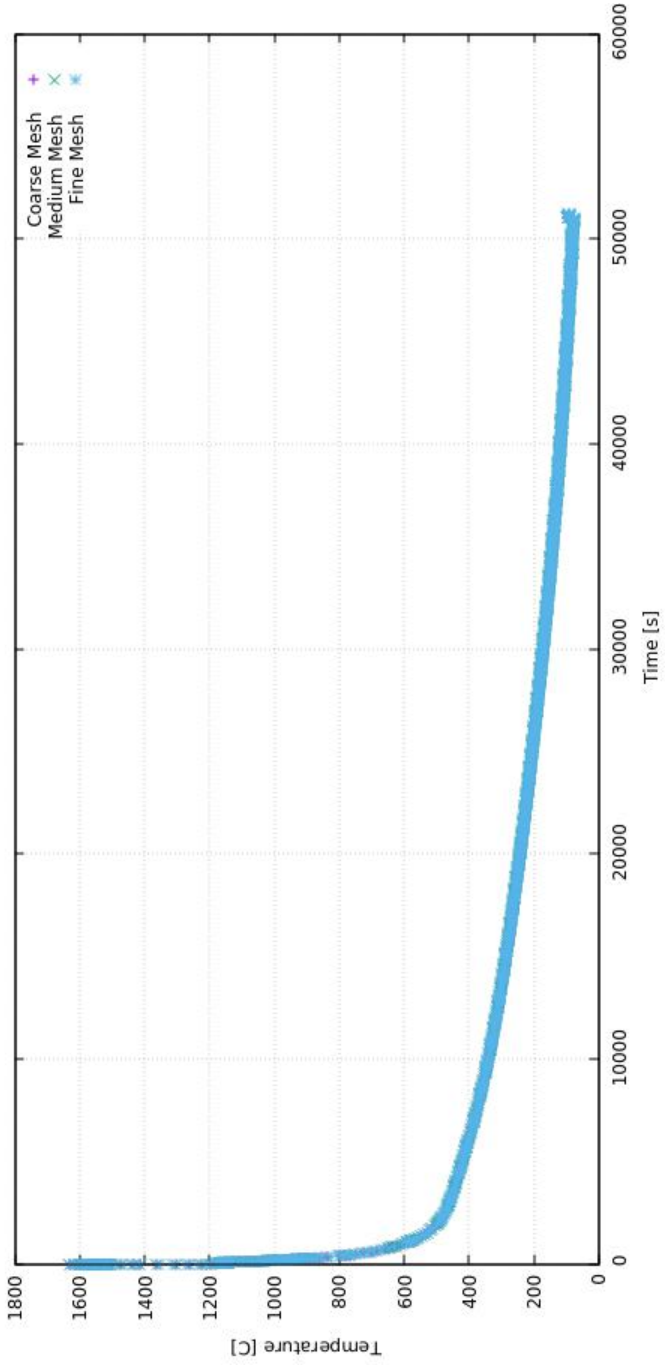

Figure B.2: Minimum temperature in casting history for three successively refined meshes

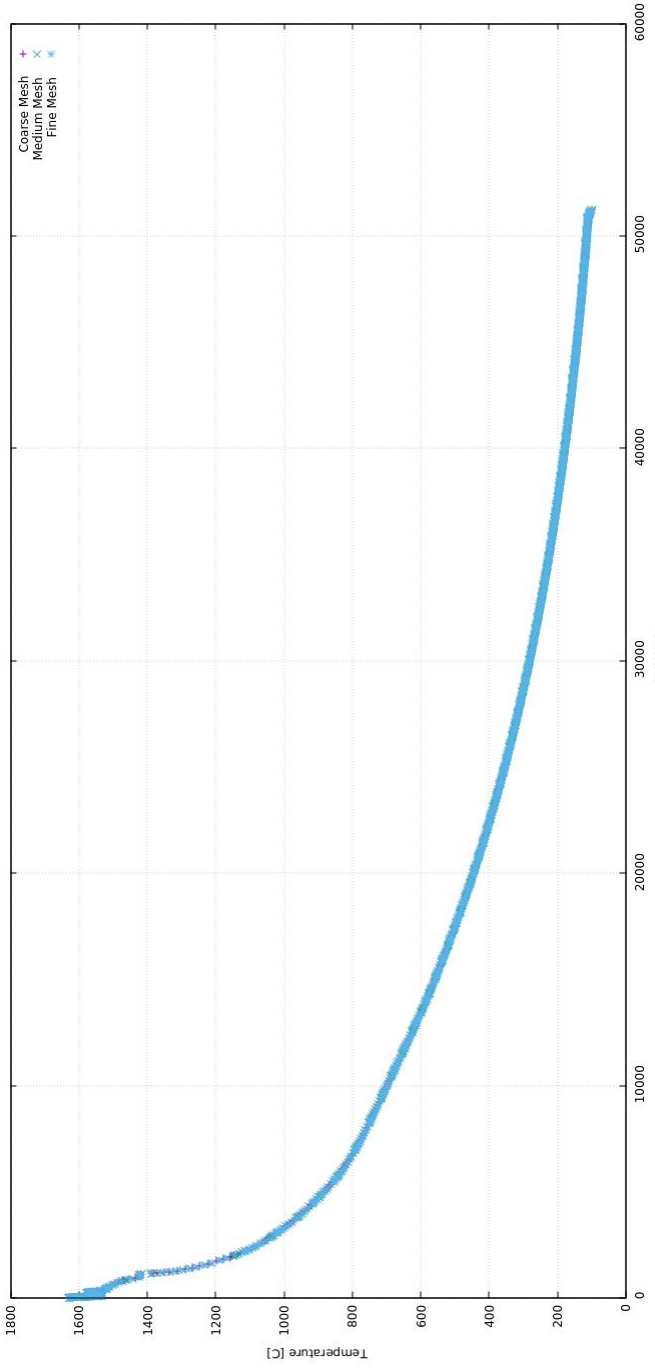

Figure B.3: Maximum temperature in casting history for three successively refined meshes

APPENDIX C - COMMERCIAL VALVE INFORMATION

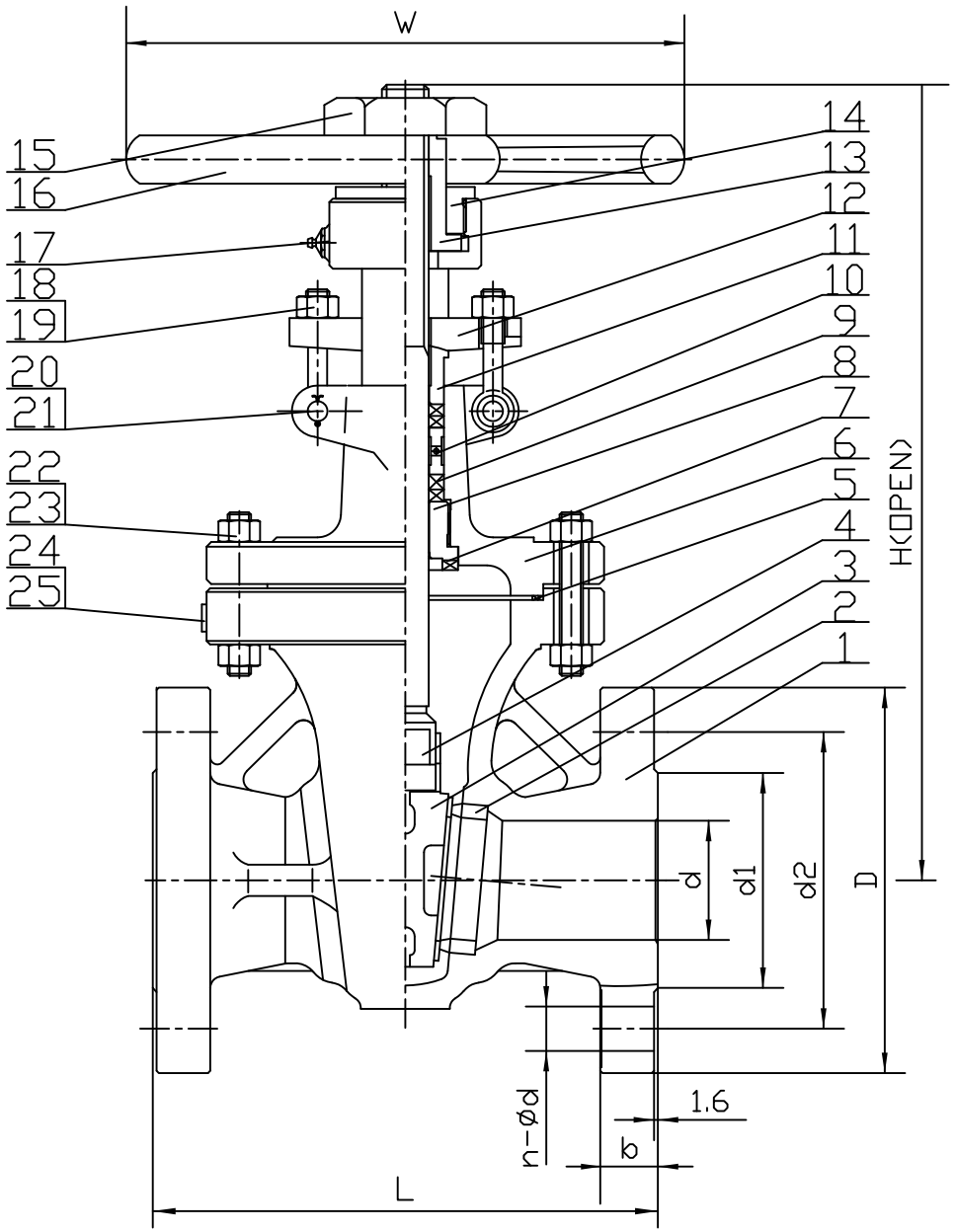

MATERIALS LIST

NO.	PART NAME	MATERIAL
1	Body	ASTM A216 WCB
2	Seat	ASTM A105+STL#6
3	Wedge	ASTM A216 WCB+F6
4	Stem	ASTM A182 F6
5	Gasket	08F+Flexible Graphite
6	Bonnet	ASTM A216 WCB
7	Back Seat	ASTM A276 410
8	Packing	Stainless Steel Wire With
9	Packing	Flexible Graphite
10	Distance Ring	ASTM A276 410
11	Gland	ASTM A276 410
12	Gland Flange	ASTM A216 WCB
13	Stem Nut	ASTM A493 D-2
14	Gland Nut	ASTM A29 1035
15	Handwheel	ASTM A536(60-40-18)
16	Lock Nut	ASTM A29 1035
17	Oillfiller	ASTM A570 Gr.A
18	Eye Bolt	ASTM A193 B7
19	Eye Nut	ASTM A194 2H
20	Pin	ASTM A29 1035
21	Split Pin	ASTM A570 Gr.A
22	Bolt	ASTM A193 B7
23	Nut	ASTM A194 2H
24	Name Plate	ASTM A276 304
25	Rivet	ASTM A276 304

FLANGE DIMENSION: ASME B16.5
FACE TO FACE: ASME B16.10

DIMENSIONS

unit:mm

SIZE	d	L	d1	d2	D	b	n-Ød	H(OPEN)	W
2"	51	216	92	127	165	23	8-19	417	200
2.5"	64	241	105	149	190	26	8-22	460	200
3"	76	283	127	168.5	210	29	8-22	526	250
4"	102	305	157	200	254	32	8-22	650	250
5"	127	381	186	235	279	35	8-22	694	300
6"	152	403	216	270	318	37	12-22	824	350
8"	203	419	270	330	381	42	12-25	987	400
10"	254	457	324	387.5	445	48	16-29	1192	450
12"	305	502	381	451	521	51	16-32	1431	500
14"	337	762	413	514.5	584	54	20-32	1559	560
16"	387	838	470	571.5	648	58	20-35	1758	640
18"	432	914	533	628.5	711	61	24-35	1942	640
20"	483	991	584	686	775	64	24-35	2145	720
22"	533	1092	641.5	743	838	70	24-41	2616	720
24"	584	1143	692	813	914	70	24-41	2904	760

Terofox Valve

CODE	DRAWING NO.	DESCRIPTION	APPROVED BY	CHECK BY	DRAWN BY	REVISION	MATERIAL	UNIT
F-002	GVF-300	API 600 GATE VALVE,TRIM 8,RISING STEM, NON RISING HANDWHEEL DESIGN,O.S &YOKE,FLEXIBLE WEDGE,ANSI CLASS 300.	PRESTON	ANITA	ANITA	00030A	MATERIALS LIST	mm

APPENDIX D - SEM ELEMENTAL ANALYSIS

Polished Sample 1

Result Type	Weight %							
Statistics	C	O	Si	P	S	Cr	Mn	Fe
Max	84.4	14.74	0.36	0.08	2.59	0.23	4.24	98.13
Min	0.88	0	0	0	0	0	0.03	0.83
Average	4.6	0.65	0.29	0.04	0.21	0.15	0.82	93.24
tandard Deviation	16.63	2.94	0.06	0.03	0.59	0.04	1	19.32

Spectrum Label	Spectrum 6	Spectrum 7	Spectrum 8	Spectrum 9	Spectrum 10	Spectrum 11	Spectrum 12	Spectrum 13	Spectrum 14	Spectrum 15
C	1.14	1.33	1.66	1.36	1.5	84.4	1.2	0.93	1.08	1.09
O	0	0.14	0	0	0	14.74	0.86	0.15	0	0
Si	0.31	0.34	0.3	0.28	0.32	0	0.36	0.31	0.28	0.32
P	0.05	0.04	0.04	0.07	0.04	0	0.07	0.05	0.04	0.06
S	0.05	0	0	0	0.28	0	0	0	0	0
Cr	0.18	0.13	0.13	0.18	0.12	0	0.21	0.17	0.19	0.16
Mn	0.48	0.38	0.55	0.48	0.81	0.03	0.52	0.58	0.49	0.48
Fe	97.79	97.64	97.31	97.63	96.94	0.83	96.79	97.81	97.93	97.88
Total	100	100	100	100	100	100	100	100	100	100

Polished Sample 1

Spectrum 16	Spectrum 17	Spectrum 18	Spectrum 19	Spectrum 20	Spectrum 21	Spectrum 22	Spectrum 23	Spectrum 24	Spectrum 25	Spectrum 26
1.17	1.52	1.25	1.51	1.79	1.26	1.29	1.1	1.37	0.88	1.12
0	0.21	0	0	0.15	0	0	0	0	0	0
0.28	0.3	0.3	0.31	0.23	0.29	0.29	0.31	0.31	0.3	0.29
0	0.06	0	0	0.06	0.04	0.06	0	0.08	0.05	0.06
2.59	0.3	0.03	1.5	0.56	0	0	0	0	0	0
0.17	0.16	0.18	0.23	0.17	0.11	0.18	0.15	0.16	0.18	0.14
4.24	0.81	0.22	3.86	1.52	0.58	0.47	0.51	0.48	0.46	0.53
91.56	96.64	98.02	92.6	95.5	97.71	97.71	97.93	97.61	98.13	97.86
100	100	100	100	100	100	100	100	100	100	100

Polished Sample 1

Spectrum 27	Spectrum 28	Spectrum 29	Spectrum 30
1.14	1.33	1.39	1.17
0	0	0	0
0.28	0.32	0.3	0.26
0.05	0	0	0
0	0	0	0
0.13	0.11	0.17	0.15
0.49	0.52	0.48	0.56
97.91	97.72	97.67	97.85
100	100	100	100

Polished Sample 2

Result Type	Oxide %									
Statistics	C	O	Si	P	S	Cr	Mn	Fe		
Max	13.16		0.49	0.14	0.08	0.31	0.87	94.75		
Min	4		0.24	0	0	0.15	0.4	85.49		
Average	6.17		0.42	0.06	0	0.19	0.53	92.62		
tandard Deviation	2.52		0.07	0.05	0.02	0.04	0.13	2.58		

Spectrum Label	Spectrum 31	Spectrum 32	Spectrum 33	Spectrum 34	Spectrum 35	Spectrum 36	Spectrum 37	Spectrum 38	Spectrum 39	Spectrum 40
C	4.57	4.55	4.22	4.51	5.33	6.46	5.23	4.79	6.37	11.6
O										
Si	0.45	0.43	0.41	0.45	0.44	0.39	0.46	0.44	0.45	0.3
P	0.08	0.14	0.09	0	0	0	0.07	0.09	0	0
S	0	0	0	0	0	0	0	0	0	0
Cr	0.2	0.2	0.19	0.15	0.15	0.2	0.18	0.2	0.24	0.31
Mn	0.44	0.52	0.51	0.44	0.54	0.54	0.52	0.59	0.52	0.87
Fe	94.27	94.16	94.59	94.45	93.55	92.4	93.54	93.89	92.43	86.92
Total	100	100	100	100	100	100	100	100	100	100

Polished Sample 2

Spectrum 41	Spectrum 42	Spectrum 43	Spectrum 44	Spectrum 45	Spectrum 46	Spectrum 47	Spectrum 48	Spectrum 49	Spectrum 50	Spectrum 51
8.71	4.08	5.08	6.26	5.14	5.36	4	5.31	5.13	9.75	13.16
0.46	0.49	0.46	0.46	0.43	0.47	0.45	0.41	0.49	0.3	0.24
0	0.07	0.06	0.06	0.09	0.13	0.09	0.12	0.09	0.08	0
0	0	0.08	0	0	0	0	0	0	0	0
0.17	0.16	0.16	0.17	0.16	0.19	0.22	0.16	0.19	0.27	0.24
0.61	0.45	0.44	0.43	0.45	0.4	0.49	0.45	0.43	0.64	0.87
90.05	94.75	93.72	92.62	93.74	93.45	94.75	93.55	93.65	88.97	85.49
100	100	100	100	100	100	100	100	100	100	100

Unpolished sample

Result Type	Weight %										
Statistics	C	O	Na	Mg	Al	Si	P	S	Cl	K	Ca
Max	36.86	49.81	0.74	8.33	2.13	5.58	0.12	0.58	0.32	0.28	5.54
Min	4.56	26.08	0.53	1.6	0.69	0.16	0.08	0	0.28	0.25	0.47
Average	23.3					2.42					
tandard Deviation	13.92					2.21					

Spectrum Label	Spectrum 52	Spectrum 54	Spectrum 55	Spectrum 56	Spectrum 57	Spectrum 58
C	7.17	4.56	36.86	29.97	33.95	27.32
O			26.08	47.39	49.81	40.09
Na			0.74	0.53		0.61
Mg			1.6	4.92	7.31	8.33
Al			1.81	2.13	0.69	0.96
Si	0.25	0.16	4.46	5.58	2.09	1.96
P	0.08			0.12		
S	0		0.08	0.58		
Cl			0.28	0.32		0.29
K			0.25	0.28		
Ca			0.52	5.54	0.57	0.47
Ti			0.08	0.08		
Cr	0.14		0.13			
Mn	0.43	0.33	0.62	0.47	0.78	1.62
Fe	91.68	94.95	26.22	1.79	4.81	18.35
Cu	0.26					
Zn			0.28	0.29		
Total	100	100	100	100	100	100

Unpolished sample

Ti	Cr	Mn	Fe	Cu	Zn
0.08	0.14	1.62	94.95	0.26	0.29
0.08	0.13	0.33	1.79	0.26	0.28
		0.71	39.63		
		0.47	42.54		